Title: Loss of Piccolo function in rats induces Pontocerebellar Hypoplasia type 3-like phenotypes

Abbreviated title: *Piccolo loss of function triggers PCH3 phenotypes*

Author names and affiliations:

Joanne Falck[1], Christine Bruns[1], Sheila Hoffmann[1], Isabelle Straub[2], Erik J. Plautz[3], Marta Orlando[4], Humaira Munawar[5], Marion Rivalan[4,5], York Winter[4,5], Zsuzsanna Izsvák[6], Dietmar Schmitz[4], F. Kent Hamra[7], Stefan Hallermann[2], Craig Garner[1*] and Frauke Ackermann[1*]

1) German Center for Neurodegenerative Diseases (DZNE), Charité Medical University, Charitéplatz 1, 10117 Berlin, Germany

2) Carl-Ludwig Institute for Physiology, 04103, Leipzig, Germany

3) Department of Neurology and Neurotherapeutics, University of Texas Southwestern, Dallas Texas 75390

4) Charité Medical University Berlin, corporate member of Free University Berlin and Humboldt University Berlin; Berlin Institute of Health, NeuroCure Cluster of Excellence, Charitéplatz 1, 10117 Berlin, Germany

5) Department of Biology, Humboldt University, Philippstr. 13, 10099 Berlin, Germany

6) Max Delbrück Center for Molecular Medicine in the Helmholtz Society, 13125, Berlin, Germany

7) Department of Obstetrics and Gynecology, Cecil H. & Ida Green Center for Reproductive Biology Sciences, University of Texas Southwestern, Dallas Texas 75390

*equal contribution

Corresponding author email address: Frauke Ackermann: frauke.ackermann@dzne.de and Craig Garner: craig.garner@dzne.de, German Center for Neurodegenerative Diseases (DZNE), Charité Medical University, Charitéplatz 1, 10117 Berlin, Germany.

Conflict of interest statement: The authors declare no competing financial interests.

Number of pages: 46

Number of figures: 9

Number of words: abstract 248, introduction 609, discussion 1499

Acknowledgments: We would like to thank Susanne Wegmann and Eckart Gundelfinger for discussion and valuable comments on the manuscript; Anny Kretschmer and Katja Czieselsky for technical assistance. The work was supported by German Center for Neurodegenerative Diseases (DZNE), the Federal Government of Germany (DFG) SFB958 to CCG and (DFG) EXC 257 for the Center of Excellence NeuroCure to YW. Work to generate *Pclo*$^{gt/gt}$ rats was supported by National institute of Health R24RR03232601 & R24OD011108 to FKH. Neurological analyses on Piccolo mutant rats were conducted by The Neuro-Models Facility (EJP, LBG) at UT Southwestern Medical Center, and supported by the Haggerty Center for Brain Injury and Repair.

Author contributions: J. Falck performed the majority of the experiments and analyzed data. J. Falck, F. Ackermann, F. K. Hamra, S. Hallermann and C. C. Garner designed experiments. M. Orlando performed electron microscopy studies, I. Straub performed electrophysiology experiments and C. Bruns performed Western Blot studies and a portion of the immunohistochemical stainings. Behavioral experiments were performed by E. J. Plautz; Behavioral experiments were performed by E. J. Plautz. and F. K. Hamra. Behavioral experiments and analysis in the OptiMan setup were performed by H. Munawar, M. Rivalan and

Y. Winter, Z. Izsvák generated *Pclo*$^{gt/gt}$ rat. J. Falck, S. Hoffmann, C.C. Garner and F. Ackermann wrote the manuscript.

Abstract

Piccolo, a presynaptic active zone protein, is best known for its role in the regulated assembly and function of vertebrate synapses. Genetic studies suggest a further link to several psychiatric disorders as well as Pontocerebellar Hypoplasia type 3 (PCH3), although a causal relationship is lacking. We have characterized recently generated knockout (*Pclo*$^{gt/gt}$) rats. Analysis revealed a dramatic reduction in brain size compared to wildtype (*Pclo*$^{wt/wt}$) animals, attributed to a decrease in the size of the cerebral cortical, cerebellar and pontine regions. Analysis of the cerebellum and brainstem revealed a reduced granule cell (GC) layer and a reduction in size of pontine nuclei. Moreover, the maturation of mossy fiber (MF) afferents from pontine neurons and the expression of the α6 $GABA_A$ receptor subunit at the MF-GC synapse are perturbed, as well as the innervation of Purkinje cells by cerebellar climbing fibers (CFs). Ultrastructural and functional studies revealed a reduced size of MF boutons, with fewer synaptic vesicles and altered synaptic transmission. These data imply that Piccolo is required for the normal development, maturation and function of neuronal networks formed between the brainstem and cerebellum. Consistently, behavioral studies demonstrated that adult *Pclo*$^{gt/gt}$ rats display impaired motor coordination, despite adequate performance in tasks that reflect muscle strength and locomotion. Together these data suggest that loss of Piccolo function in patients with PCH3 could be causal for many of the observed anatomical and behavioral symptoms, and that the further analysis of these animals could provide fundamental mechanistic insights into this devastating disorder.

Key Words: presynapse, active zone, Piccolo, Pontocerebellar hypoplasia

Significance Statement: Pontocerebellar Hypoplasia type 3 is a devastating developmental disorder associated with severe developmental delay, progressive microcephaly with brachycephaly, optic atrophy, seizures and hypertonia with hyperreflexia. Recent genetic studies

have identified non-sense mutations in the coding region of the Piccolo gene, suggesting a functional link between this disorder and the presynaptic active zone. Our analysis of Piccolo knockout rats supports this hypothesis, formally demonstrating that anatomical and behavioral phenotypes seen in patients with PCH3 are also exhibited by these Piccolo deficient animals.

Introduction

Pontocerebellar Hypoplasia is a rare and highly heterogeneous group of neurological disorders, often with a genetic origin, characterized by an abnormally small cerebellum and pons (Rajab et al., 2003; Namavar et al., 2011). In type 3 Pontocerebellar Hypoplasia (PCH3) - also known as Cerebellar Atrophy with Progressive Microcephaly (CLAM) - patients suffer from severe developmental delay, progressive microcephaly with brachycephaly, seizures, hypertonia with hyperreflexia and short stature (Rajab et al., 2003; Namavar et al., 2011). Additional features include the presence of craniofacial dysmorphisms and optic atrophy (Durmaz et al., 2009; Rudnik-Schoneborn et al., 2014).

Previous studies mapped the PCH phenotype to chromosome 7q11-21 (Rajab et al., 2003; Durmaz et al., 2009). More recently, a single nucleotide polymorphism (SNP) in the human *Pclo* gene - indeed, located on chromosome 7 at position 21.11 - has been found in patients with PCH3. This non-sense mutation is predicted to eliminate the C-terminus of the longest Piccolo isoforms including its PDZ and C2 domains (Ahmed et al., 2015) and perhaps destabilize the protein, leading to the hypothesis that Piccolo loss of function is responsible for the phenotypes seen in this neurodevelopmental/neurodegenerative disorder.

Piccolo is a very large (560kDa) multidomain presynaptic scaffold protein and core component of the cytoskeletal matrix assembled at active zones (CAZ) (Cases-Langhoff et al., 1996). A range of studies suggest that Piccolo uses its multidomain structure to scaffold not only other CAZ proteins critical for the regulated release of neurotransmitters, but also proteins involved in the dynamic assembly of F-actin, synaptic vesicle (SV) recycling and synapse

integrity (Gundelfinger et al., 2015; Ackermann et al., 2019). Intriguingly, Piccolo is present at nearly every synaptic subtype including glutamatergic, GABAergic, cholinergic and dopaminergic synapses within the central (CNS) and peripheral nervous system (PNS) (Cases-Langhoff et al., 1996; Fenster et al., 2000; Fenster and Garner, 2002) and is highly expressed in the cerebrum, hippocampus, cerebellum and olfactory bulb, among others (Cases-Langhoff et al., 1996; Human Protein Atlas, 2015) . It is one of the very first active zone (AZ) proteins recruited to nascent synapses *in vitro* as well as in the developing brain (Zhai et al., 2001). For example, Piccolo appears at emerging synapses formed between mossy fiber boutons and cerebellar granule cells as well as between parallel fiber boutons and Purkinje cell dendrites during the earliest stages of cerebellar development (Zhai et al., 2001). The large size of Piccolo and the complexity of the *Pclo* gene has thwarted most efforts to elucidate its function, though critical roles in retinal ribbon synapse formation and visual function (Regus-Leidig et al., 2014; Muller et al., 2019) as well as the integrity of hippocampal synapses has been identified (Waites et al., 2013). What remains unclear is how Piccolo contributes to cerebellar development and whether, as suggested by genetic studies, it has a primary role in the etiology of PCH3. The recent generation of a Piccolo knockout rat ($Pclo^{gt/gt}$) using transposon mutagenesis (Medrano et al., 2019) provides an opportunity to explore this potential relationship.

In the current study, we have assessed the contribution of Piccolo to cerebellar structure and function through the anatomical, functional and behavioral characterization of adult $Pclo^{gt/gt}$ rats. Our analysis reveals a striking number of similarities to patients with PCH3, including a smaller cerebral cortex, a reduced volume of the cerebellum and pons as well as impaired motor control and the presence of seizures. Our analysis has also uncovered changes in the anatomical and ultrastructural features of mossy fiber terminals and electrophysiological properties of these synapses. Together, these phenotypes are predicted to not only alter the functionality of the cerebellum but to contribute to motor and perhaps also behavioral dysfunctions seen in PCH3 affected individuals.

Results

Brain morphology is changed in Piccolo knockout brains.

The recent analysis of a pair of boys with PCH3 identified a non-sense mutation in the coding region of the human *Pclo* gene (chr7:82579280 G>A), predicted to eliminate the C-terminal third of the longest Piccolo isoforms (Ahmed et al., 2015) and likely its expression. These individuals have profound cognitive and motor impairment as well as atrophy of the cerebrum, cerebellum and pons (Ahmed et al., 2015). A fundamental question is whether Piccolo loss of function is causal for this disorder. To explore this possibility, we have characterized a recently generated line of rats ($Pclo^{gt/gt}$) wherein transposon mutagenesis was used to disrupt the Piccolo gene via an insertion into exon 3 (Figure 1A). This insertion is predicted to cause a frame shift in the reading frame and thus disrupt the expression of full-length Piccolo (560kDa) and most of its alternatively spliced lower molecular weight isoforms (70-350kDa). Schematic is adapted from Ackermann et al. (Ackermann et al., 2019; Medrano et al., 2019). Just after birth (P0-P2) Piccolo pups were found born in normal Mendelian numbers (Figure 1B). Western blot analysis of brain lysates from postnatal day 0-2 (P0-P2) pups demonstrates the loss of nearly all isoforms in homozygous knockout animals (Figure 1C). To assess whether Piccolo loss of function adversely affects brain development, we performed an anatomical characterization of $Pclo^{wt/wt}$ and $Pclo^{gt/gt}$ animals; $Pclo^{gt/gt}$ pups were smaller and weighed significantly less than their $Pclo^{wt/wt}$ littermates (Figure 1D, E and F). However, brain weights were not significantly altered between $Pclo^{gt/gt}$ and $Pclo^{wt/wt}$ littermates at P0-2 and display similar brain morphology (Figure 1G, H and I), suggesting that changes in brain size develop postnatally. However, the overall size and weight of $Pclo^{gt/gt}$ brains was significantly reduced in 3 month-old adult rats compared to $Pclo^{wt/wt}$ brains (Figure 1J and K). To assess whether this was associated with an overall loss in brain volume or due to reductions in specific brain regions, serial sagittal and coronal sections from 3 month-old animals were collected and stained with Nissl to visualize brain morphology (Figure 1L). Qualitative analysis revealed that thalamic, cerebellar and brainstem regions are dramatically reduced in size

105 in 3 month-old *Pclo*$^{gt/gt}$ animals. Some thinning of the cerebral cortex can also be observed,
106 however, no obvious changes in the hippocampus are detectable. Furthermore, ventricles (V1,
107 V2, V3 and V4) in *Pclo*$^{gt/gt}$ brains were all notably larger than in *Pclo*$^{wt/wt}$ littermates (Figure 1L).

108 Intriguingly, the observed morphological changes in brains of 3 month-old *Pclo*$^{gt/gt}$
109 animals are remarkably similar to those reported for patients with PCH3, who exhibit
110 microcephaly, a reduced size of the cerebrum, cerebellum and pons as well as larger ventricles
111 (Maricich et al., 2011). As hypoplasia of the pons and cerebellum as well as a reduced thickness
112 of the cortex are the most dramatic features of PCH3 patients, we examined in more detail
113 changes occurring in these regions of *Pclo*$^{gt/gt}$ brains. Here, we found that the thickness of the
114 cortex is significantly reduced in brains lacking Piccolo (Figure 2A and D). The area of the pons
115 is dramatically reduced in *Pclo*$^{gt/gt}$ brain slices stained with Nissl (Figure 2B). As the density of
116 neurons was not changed (Figure 2B, zoom), these data indicate a loss of the total number of
117 neurons within the pons. This conclusion is supported by data from brainstem sections stained
118 with antibodies against the synaptic vesicle (SV) protein VGluT1, prominently expressed in pons
119 neurons, which reveals a smaller area occupied by these neurons (Figure 2C and E).

120 Analysis of sagittal sections through the cerebellum of adult rats reveals that, whilst the
121 cerebellum is smaller in *Pclo*$^{gt/gt}$ animals, the overall anatomy is not altered (Figure 3A). For
122 example, there are no remarkable defects in foliation of *Pclo*$^{gt/gt}$ animals, with all lobes present
123 and appearing to be formed normally at the vermis (Figure 3A and E). Our analysis of the granule
124 cell layer (GCL), using DAPI to stain granule cell (GC) nuclei, reveals that this layer is
125 significantly reduced in size in *Pclo*$^{gt/gt}$ compared to *Pclo*$^{wt/wt}$ controls (Figure 3A and C).
126 However, this decrease was not associated with a proportional increase in GC packing density, as
127 the number of GCs per GCL area is only very slightly increased (Figure 3B and D). These data
128 indicate an overall loss of GCs in *Pclo*$^{gt/gt}$ cerebella. Conceptually, this is predicted to reduce the
129 total number of GC parallel fibers innervating PC dendrites in the molecular layer (ML), a

130 situation that could lead to a thinner ML and perhaps an altered packing density of Purkinje cells
131 (PCs).

132 Sections immunostained with antibodies against Calbindin, which specifically labels PCs,
133 reveals that the organization of the ML and the PC layer (PCL) appear to be intact and that the
134 dendritic arbors of PCs are correctly orientated (Figure 3E, F and I). However, quantifying the
135 average area per unit length of the ML reveals a dramatic reduction in the size of this layer in
136 *Pclo*$^{gt/gt}$ brains (Figure 3G). Furthermore, cells in the PCL appear overcrowded in *Pclo*$^{gt/gt}$
137 cerebella (Figure 3E, F and I), a conclusion supported by data showing an increased packing
138 density of PCs in *Pclo*$^{gt/gt}$ brains (Figure 3H).

139 Taken together, these data indicate a reduced number of GCs and a higher packing
140 density of PCs in *Pclo*$^{gt/gt}$ cerebella compared to *Pclo*$^{wt/wt}$ controls.

141

142 **Loss of Piccolo alters climbing fiber and mossy fiber innervation in the cerebellum.**

143 Anatomically, the cerebellum receives its major excitatory afferents in the form of
144 climbing fibers (CFs) and mossy fibers (MFs) that project from the inferior olive or the
145 brainstem/spinal cord, respectively (Leto et al., 2016). Both form glutamatergic synapses but
146 terminate in different layers of the cerebellum (Apps and Garwicz, 2005). For example, CFs form
147 excitatory synapses onto the proximal branches of PC dendritic arbors, modulating the dynamic
148 firing properties of PCs and motor learning (Hashimoto and Kano, 1998). In contrast, MFs
149 terminate on the dendrites of GCs, which then provide direct excitatory input to PCs via their
150 parallel fiber (PF) axons. Both also extend collaterals to the deep cerebellar nuclei before
151 projecting into the cerebellar cortex (Shinoda et al., 1992).

152 In previous studies, we observed that Piccolo was present in the boutons of each of these
153 excitatory synapses (Cases-Langhoff et al., 1996). This was confirmed by immunostaining
154 cerebellar sections of *Pclo*$^{wt/wt}$ and *Pclo*$^{gt/gt}$ with antibodies against Piccolo and the SV protein
155 VGlut1 (Fig. 4A and B). This revealed that Piccolo immuno-reactivity was indeed present at each

156 of these synaptic types and that this immuno-reactivity was lost in cerebella from *Pclo*$^{gt/gt}$
157 animals. To explore whether deficiencies in either could contribute to the anatomical and
158 functional changes in the cerebellum, we initially analyzed potential differences in the CF input
159 into the ML. Synaptic input from CFs onto PC dendrites, immuno-positive for Calbindin, was
160 visualized with antibodies against VGluT2 (Miyazaki et al., 2003). Here our analysis of sagittal
161 sections revealed the presence of a large number of VGluT2 positive puncta decorating Calbindin
162 positive dendrites in *Pclo*$^{gt/gt}$ and *Pclo*$^{wt/wt}$ sections (Figure 4C and D). These data indicate that the
163 loss of Piccolo does not affect the ability of CFs to project into the ML and form synapses with
164 PC soma and dendrites. Qualitatively, VGluT2 positive puncta in *Pclo*$^{wt/wt}$ and *Pclo*$^{gt/gt}$ sections
165 were of similar size and beautifully decorated both primary and tertiary PC dendrites, though the
166 total number of puncta appeared more numerous in *Pclo*$^{gt/gt}$ sections. Quantification of the total
167 area of VGluT2 per ML supports this impression (Figure 4D). Additionally, we compared the
168 distribution of the CFs to the synaptic inputs from GCs onto PCs, the parallel fiber (PF) axons
169 which project into the ML. The latter synapses were identified with antibodies against VGluT1
170 (Miyazaki et al., 2003). Although the ML is thinner in *Pclo*$^{gt/gt}$ cerebella (Figure 3A), we
171 observed no overt changes in the intensity or distribution of VGluT1 positive puncta throughout
172 the ML of *Pclo*$^{gt/gt}$ animals compared to *Pclo*$^{wt/wt}$ controls (Figure 4C). This implies that PF axons
173 project normally and form a robust number of synapses with PCs. Given that fewer GCs are
174 formed in *Pclo*$^{gt/gt}$ cerebella (Figure 3A and B), we postulate that the thinner ML is most likely
175 due to fewer PFs and less total synaptic input on PC dendrites.

176 GCs are known to receive their excitatory input from MFs arising from afferent axons
177 from a number of distinct nuclei in the brainstem including the pontine nuclei (Sillitoe, 2012).
178 These collaterals form large glomerular structures with multiple AZs, forming a rosette of
179 synapses with claws from dendrites of multiple GCs (Jakab and Hamori, 1988; Xu-Friedman and
180 Regehr, 2003). Given the smaller size of the pons, we thus explored whether the boutons from the
181 remaining cells properly reached the cerebellum and formed robust MF terminals. As afferent

182 fibers from the pons primarily innervate cerebellar lobes VI to IX, we examined sagittal sections
183 of these lobes stained with antibodies against the somatodendritic marker MAP2 and VGluT2 in
184 lobe VII. In *Pclo*$^{wt/wt}$ sections, multiple large VGluT2 positive puncta are seen packed tightly
185 together within a dense meshwork of MAP2 positive dendrites projecting from a ring of GCs.
186 These puncta represent subclusters of SVs with large 100-200 μm^3 terminals (Jakab and Hamori,
187 1988). In sections from *Pclo*$^{gt/gt}$ animals, each bouton appeared smaller in size and less organized,
188 though they still appear to contact GC dendrites (Figure 5A). This impression is further supported
189 by sections immunostained with antibodies against VGluT1 and VGluT2. In these images,
190 distinct VGluT1 and/or VGluT2 positive clusters are observed in both *Pclo*$^{wt/wt}$ and *Pclo*$^{gt/gt}$
191 animals, consistent with individual boutons or glomeruli (Figure 5B). Here again, MF terminals
192 from *Pclo*$^{gt/gt}$ animals appeared to have much smaller VGluT1 or VGluT2 positive clusters
193 (Figure 5B, zoom). Quantifying the average size of the VGluT1 and VGluT2 positive clusters
194 revealed that clusters of *Pclo*$^{wt/wt}$ cerebella were more than double the size compared to the same
195 lobes in *Pclo*$^{gt/gt}$ animals (Figure 5B and C). However, this effect was not lobe-specific as it was
196 observed in all lobes and not just in those receiving pontocerebellar afferents (Figure 5B). These
197 findings suggest that defects in the formation of large robust MF glomeruli in *Pclo*$^{gt/gt}$ cerebella is
198 a common feature shared by MF afferents arising from the pons and other brainstem nuclei, and
199 may reflect aberrant signaling during development between GCs and these neurons.

200 Quantitatively, the spread of distribution of VGluT1 and VGluT2 cluster sizes is far more
201 shifted towards smaller cluster sizes in *Pclo*$^{gt/gt}$, with mutant cerebellar displaying approximately
202 45 % more small synaptic clusters of 5 μm^2 in size than *Pclo*$^{wt/wt}$ counterparts (Figure 5D). At the
203 larger end of the scale, cluster sizes over 50 μm^2 were much more frequent for *Pclo*$^{wt/wt}$ than
204 *Pclo*$^{gt/gt}$ cerebella (Figure 5E).

205 In addition to excitatory input, MF glomeruli are also modulated by GABAergic
206 inhibition via cerebellar Golgi cells, which offer regulatory feedback to the complex, as they
207 themselves are excited by GCs (Maex and De Schutter, 1998). In principle, smaller MFs

208 terminals seen in Piccolo KO animals could represent less excitatory input into GCs. This may
209 also reduce excitatory drive onto PCs via PFs from GCs, as well as perhaps inhibitory drive via
210 the Golgi cells. One of the dominant receptors mediating inhibitory input from Golgi cells to GCs
211 are the α6 subunit-expressing $GABA_A$ receptors, which are highly concentrated within MF
212 glomeruli (Nusser et al., 1996). Sagittal sections immunostained with antibodies against VGluT2
213 and α6 subunits revealed that the $GABA_A$ α6 receptor subunit is only weakly expressed in *Pclo*$^{gt/gt}$
214 MF rosettes, whereas in *Pclo*$^{wt/wt}$, it nicely localizes to the synaptic complex (Figure 6A).
215 Antibody staining of the granule cell layer demonstrates higher intensity of $GABA_A$ α6 antibody
216 staining in *Pclo*$^{wt/wt}$ compared to *Pclo*$^{gt/gt}$ (Figure 6B). However, knockout models of $GABA_A$α6
217 (Homanics et al., 1997) do not display PCH3 phenotypes or alterations in the anatomy of the
218 cerebellum. Therefore, $GABA_A$α6 downregulation can be attributed to Piccolo loss and not for
219 the PCH3 phenotypes.

220 These data suggest that the loss of Piccolo not only affects the size of MF inputs into the
221 cerebellum, but also gene expression and therefore inhibitory drive within each glomerulus, a
222 condition that could relate to the maturation of these structures and/or their functionality, a
223 situation that could adversely affect cerebellar function.

224

225 **Ultrastructural analysis of mossy fiber glomeruli in *Pclo*$^{gt/gt}$ cerebellum.**

226 The reduced area of VGluT1 and VGluT2 clusters within *Pclo*$^{gt/gt}$ MF terminals (Figure
227 6) could be due to a reduction in size of MF glomeruli themselves and/or in the number of
228 VGluT1/2 positive SVs per bouton. To explore these options, we investigated MF glomeruli in
229 *Pclo*$^{wt/wt}$ and *Pclo*$^{gt/gt}$ cerebella using electron microscopy (EM). Analysis of ultrathin cerebellar
230 brain sections from 3 month-old rats revealed that the average size of *Pclo*$^{gt/gt}$ glomeruli was
231 significantly smaller than *Pclo*$^{wt/wt}$ glomeruli (Figure 7A and C). Furthermore, the complexity of
232 the glomeruli indicated by a P2A value, measuring the ratio of perimeter per area, was
233 significantly reduced (Figure 7E). The size of the presynaptic area was also reduced in *Pclo*$^{gt/gt}$

234 cerebellar sections (Figure 7B and D). However, the number of active zones (AZs) present at
235 each glomerulus was still proportional to their size, as *Pclo*$^{wt/wt}$ and *Pclo*$^{gt/gt}$ had a similar number
236 of AZs per glomerular area (Figure 7B and F). Given that *Pclo*$^{gt/gt}$ boutons are smaller, this
237 indicates that the overall output of the MF glomeruli could be reduced in *Pclo*$^{gt/gt}$ cerebellum.
238 Intriguingly, we also noticed an accumulation of clathrin-coated vesicles (CCVs) in the terminals
239 of *Pclo*$^{gt/gt}$ MFs (Figure 7G). This phenotype resembles recent findings from hippocampal
240 synapses from *Pclo*$^{gt/gt}$ animals, which revealed defects in the formation of endosomal membranes
241 and an overall reduction in SV number (Ackermann et al., 2019) and suggest possible changes in
242 the recycling of SVs within MF boutons post fusion with the plasma membrane.
243
244 **Piccolo loss alters GC properties and mossy fiber to GC synaptic transmission**
245 The anatomical and morphological changes observed in MF boutons lacking Piccolo are
246 predicted to not only represent altered afferent input into the cerebellum from the pons and other
247 brainstem nuclei, but also altered cerebellar function. As an initial test of this hypothesis, we
248 performed whole-cell current clamp recordings of cerebellar GCs from acute P90 rat cerebellar
249 slices. A two-photon image of a typical cerebellar GC from *Pclo*$^{gt/gt}$ filled with ATTO dye reveals
250 a normal radial arrangement of its dendrites as they project their claws into MF glomeruli (Figure
251 8A). An analysis of the intrinsic biophysical properties of these cells revealed that the GC
252 properties differed between *Pclo*$^{gt/gt}$ and *Pclo*$^{wt/wt}$ animals. Specifically, no changes were detected
253 in either the capacitance or the membrane potential of these cells, but the input resistance was
254 significantly increased (Figure 8B). Since these experiments were performed in the presence of
255 $GABA_A$ receptor blockers, the decreased shunting inhibition mediated by tonic activation of α6-
256 subunit-containing $GABA_A$ receptors (Brickley et al., 1996; Nusser et al., 1998) is expected to
257 further increase the difference in input resistance. Yet, there was also no change in the amplitude,
258 threshold of activation or duration of action potentials fired by these cells (Figure 8B), indicating
259 unaltered active membrane properties. Examining the frequency and amplitude of spontaneous

260 miniature excitatory postsynaptic currents (mEPSCs) of these GCs revealed a dramatic increase
261 in the frequency of these events in *Pclo*$^{gt/gt}$ slices with no change in mEPSC amplitudes (Figure
262 8C). These data suggest that on average each excitatory synapse formed on to these GC dendrites
263 has normal levels of postsynaptic AMPA-type glutamate receptors. The change in frequency
264 could either be due to an increase in the number of MF boutons contacting GC dendrites and/or
265 an increase in the release probability of MF boutons. Consistently, the average amplitude of the
266 evoked excitatory postsynaptic currents (EPSCs) was increased in *Pclo*$^{gt/gt}$ animals, with no
267 change in the weighted time constant (τ_w) (Figure 8D). Given the amplitudes of the mEPSCs are
268 not changed, these results suggest that there is a higher number of synaptic connections between
269 MF boutons and the dendrites of GCs, consistent with the larger number of smaller SV
270 clusters/rosette in *Pclo*$^{gt/gt}$ animals (Figure 6). Taken together, these data indicate that, in addition
271 to changes in cell number, the loss of Piccolo in the cerebellum and brainstem is associated with
272 changes in the morphology and function of GCs and their mossy fiber input.
273
274 **Behavioral and motor defects in Piccolo knockout rats.**
275 The motor difficulties reported (Zelnik et al., 1996; Durmaz et al., 2009) in humans with
276 PCH3 and the anatomical changes observed in the cerebellum and brainstem of rats lacking
277 Piccolo predict altered motor function in these animals. To test this hypothesis, *Pclo*$^{wt/wt}$, *Pclo*$^{wt/gt}$
278 and *Pclo*$^{gt/gt}$ rats were monitored for their motor abilities. In rotarod tasks, *Pclo*$^{gt/gt}$ rat
279 performance was significantly reduced compared to *Pclo*$^{wt/wt}$ and *Pclo*$^{wt/gt}$ rats (Figure 9A).
280 Specifically, while *Pclo*$^{wt/wt}$ and *Pclo*$^{wt/gt}$ rats exhibited increasing performance levels regarding
281 the ability to stay on the rotarod over time, *Pclo*$^{gt/gt}$ rats showed no indication of being able to
282 adapt to the task. *Pclo*$^{gt/gt}$ rats were less adept at staying on the task apparatus once rod rotation
283 was initiated (Figure 9A). Intriguingly, no differences in forelimb grip strength were scored
284 between Piccolo genotypes (Figure 9B), indicating that *Pclo*$^{gt/gt}$ rats showed lack of motivation
285 and/or impaired coordination.

286 In addition to deficits in motor ability, *Pclo*$^{gt/gt}$ rats displayed an increased frequency in
287 front and rear foot stepping errors during ladder rung walking compared to *Pclo*$^{wt/wt}$ and *Pclo*$^{wt/gt}$
288 rats (Figure 9C). In open field tests, no significant differences were recorded between *Pclo*$^{wt/wt}$,
289 *Pclo*$^{wt/gt}$ and *Pclo*$^{gt/gt}$ rats for peripheral line crossing or self-grooming events (Figure 9D).
290 However, *Pclo*$^{gt/gt}$ rats displayed 2- to 3-fold decreases in peripheral rearing events compared to
291 *Pclo*$^{wt/wt}$ and *Pclo*$^{wt/gt}$ animals (Figure 9D). Deficits in *Pclo*$^{gt/gt}$ rat performance during rotarod,
292 ladder rung and open field tests (Figure 9A-D) reflected recessive traits, consistent with
293 dysfunction in proprioceptive sensation and motor control (Curzon et al., 2009).
294 Alongside traditional tests for motor coordination, we tested the behavior of *Pclo*$^{wt/wt}$,
295 *Pclo*$^{wt/gt}$ and *Pclo*$^{gt/gt}$ rats in a home cage setup, the OptiMan (Operator Independent Motor-
296 analysis) system, where animals can be monitored without interference from experimenters. Rats
297 were tagged with a radio frequency identification chip that allowed for tracking of locomotor
298 activity while they were also required to complete an isometric pull task that requires precise and
299 finely controlled movements. In the home cage, the *Pclo*$^{gt/gt}$ rats were more active and covered
300 about twice the distance than *Pclo*$^{wt/wt}$ rats (Figure 9E) during each measurement. In the isometric
301 pull task, performance of *Pclo*$^{gt/gt}$ rats was significantly lower than the performance of *Pclo*$^{wt/wt}$
302 rats, quantified using four different force thresholds (Figure 9F). Taken together, *Pclo*$^{gt/gt}$ rats
303 show clear motor deficits, very similar to symptoms seen in PCH3 patients (Rajab et al., 2003).
304
305 **Discussion**
306 Our study demonstrates that Piccolo LOF causes alterations in brain anatomy. In
307 particular, the cerebrum, pons, brainstem and cerebellum are severely reduced in size whereas the
308 ventricles are increased (Figure 1). These changes are associated with reductions in cerebellar and
309 pontine cell numbers and perturbations in cerebellar CF and MF afferents (Figure 4 and 5). These
310 changes are predicted to adversely affect cerebellar function - supported by changes in synaptic
311 transmission and motor control in *Pclo*$^{gt/gt}$ rats. Interestingly, the changes in brain morphology

312 resemble changes in children with PCH3, recently linked to a SNP in the PCLO gene (Ahmed et
313 al., 2015). In addition to brain atrophy, children with PCH3 have, amongst other symptoms,
314 cognitive and motor deficits as well as seizures. Given that seizures were also observed in *Pclo*$^{gt/gt}$
315 rats (Medrano et al., 2019), we postulate that *Pclo*$^{gt/gt}$ rats represent a model to study the
316 underlying mechanisms of this devastating disease.

317 Similar to patients with PCH3, *Pclo*$^{gt/gt}$ rats have smaller cerebella, brainstem and pontine
318 nuclei. In the cerebellum, a striking change was the thickness of the ML and CGL (Figure 3). The
319 latter was associated with fewer total GCs, which could result in fewer PFs and a thinner ML.
320 The orientation of PCs and the ramification of their dendritic arbors were largely unchanged. At
321 present, it is unclear why there are fewer GCs in *Pclo*$^{gt/gt}$ cerebella. During normal development,
322 several factors including Sonic hedgehog (Wallace, 1999; Miyashita et al., 2017) and Notch
323 (Solecki et al., 2001) are known to control the proliferation of GCs. How Piccolo loss influences
324 these and related signaling pathways is unclear; though Piccolo and Bassoon have been shown to
325 regulate the activity-dependent translocation of c-terminal binding protein 1 (CTPB1) to the
326 nucleus and thereby the expression of neuronal genes (Ivana et al., 2015). CTPB1 and CTPB2 are
327 highly expressed in the cerebellum and their function and/or localization could be affected by
328 Piccolo LOF (Hubler et al., 2012; Ivanova et al., 2015). There is a clear rationale for exploring
329 this phenotype further.

330 In the ML, CF morphology and arrangement appear to be normal, though a higher
331 innervation of PC dendrites by CFs can be observed (Figure 4). One possible explanation for this
332 hyper-innervation is that homeostatic changes to the network, such as heterosynaptic competition
333 with PFs for PC dendrite territory (Hashimoto et al., 2009; Ichikawa et al., 2016) could contribute
334 to these differences in CF distribution and therefore the functionality of the cerebellum. This
335 could affect normal pruning mechanisms of CF during development.

336 Our study also revealed that the pontine nuclei was dramatically decreased in size in
337 *Pclo*$^{gt/gt}$ animals. This is note-worthy as afferent MFs from the pons and other brainstem nuclei

338 are the primary excitatory input onto GCs, forming elaborate rosette synapses (Voogd and
339 Glickstein, 1998). The smaller size of the pons suggests a net reduction in MF input into the
340 cerebellum that appears to correspond to the reduced number of GCs (Figure 3). However, it is
341 unclear how the loss of Piccolo could influence the number of neurons in the pons.

342 Surprisingly, our histological studies revealed that MF boutons across all lobes of the
343 cerebellum were reduced in size (Figure 5). This finding was supported by our EM studies
344 revealing that MF glomeruli are severely reduced in size, potentially resulting in smaller SV
345 clusters (Figure 7). These observations suggest that the development/maturation of MFs from the
346 pons and other brainstem nuclei are muted in *Pclo*$^{gt/gt}$ animals. Additionally, electrophysiological
347 changes (Figure 8) indicate that the network has triggered compensatory changes to overcome a
348 smaller size or impaired strength of MFs reaching the GC layer, for instance by increasing both
349 input resistance and release probability (Turrigiano, 2012).

350 Our electron micrographs also showed what could be disturbed synaptic integrity in
351 *Pclo*$^{gt/gt}$ MF boutons with more CCVs being present (Figure 7), suggesting that the loss of Piccolo
352 may also affect SV recycling. These observations are in accordance with recent findings by
353 Ackermann et al. (2019) of hippocampal synapses from *Pclo*$^{gt/gt}$ animals. Here, it was reported
354 that the loss of Piccolo had a dramatic effect on the recycling of SV proteins through a functional
355 block in the formation of early endosomes from endocytic vesicles, due to defects in the
356 activation of Rab5 via a Piccolo-dependent loss of Pra1 from synapses. Although beyond the
357 current study, it is likely that this endocytic defect in the recycling of SV proteins could also
358 contribute to altered size function of MF synapses, especially given their high frequency
359 transmission and therefore need for high SV turnover (Byczkowicz et al., 2018).

360 GCs also receive inhibitory modulation from Golgi cells (Eccles et al., 1966) and it is
361 well appreciated that $GABA_A$ receptors at the MF synapse contain α6 subunits (Nusser et al.,
362 1996). Intriguingly, *Pclo*$^{gt/gt}$ rats display a reduced expression of the $GABA_A$α6 subunit at MF
363 rosettes (Figure 6). This is in line with findings from Medrano et al. (2019), who performed RNA

364 sequencing on the *Pclo*$^{gt/gt}$ rats and found a severe reduction in GABA$_A$α6 subunit gene
365 expression.

366 At present, it is unclear why levels of these subunits are reduced. One possibility is that it
367 reflects a homeostatic change within cerebellar circuitry to compensate for a reduced excitatory
368 input from MFs (Figure 5). This concept is supported by electrophysiological data showing that
369 the input resistance of GCs is higher as is mEPSC frequency and EPSC amplitudes (Figure 8).
370 This condition might arise to compensate for the smaller MF terminals reaching the GCL, which
371 could initially have weaker output properties. Alternatively, reduced GABA$_A$α6 expression could
372 be due to lower levels of BDNF, which is secreted from precerebellar neurons, at MF terminals
373 (Chen et al., 2016) and is necessary to promote the formation of GABAergic synapses onto GCs.
374 Though a role of Piccolo in the secretion of BDNF has not been investigated, the expression of
375 Bassoon, which shares significant functional redundancy with Piccolo, is linked to presynaptic
376 levels of BDNF (Heyden et al., 2011). In this regard, the remaining Bassoon protein could
377 suppress BDNF secretion in MF terminals, altering the maturation of the glomeruli and
378 GABA$_A$α6 expression.

379 An important question not addressed by our studies is why MF boutons are smaller. By
380 several measures mentioned above, it would appear that the MF glomeruli are less mature. Key
381 regulators of MF maturation are members of the Wnt family, a group of target-derived factors
382 which accelerate neuronal maturation or directly induce synapse formation (Scheiffele, 2003;
383 Waites et al., 2005). Interestingly, mouse cerebellar MFs lacking Wnt7a show a similar reduction
384 in MF size and complexity, as we observed in *Pclo*$^{gt/gt}$ (Hall et al., 2000). However, it is important
385 to note that in the case of Wnt7a loss, MF synapse size catches up to WT size by age P15, which
386 points to a lag in maturation and does not quite seem to be the case in our *Pclo*$^{gt/gt}$ rats. Knockout
387 of Disheveled1 (Dvl1), a downstream target of Wnt (Salinas and Zou, 2008) also shows a
388 reduction in MF cluster size, indicating that presynaptic Dvl1 is a necessary step in the Wnt
389 signaling cascade, underscoring the importance of these proteins for MF-GC synapse formation

390 (Ahmad-Annuar et al., 2006). Like Dvl1, Piccolo is located at the AZ of the presynaptic terminal
391 and regulates F-actin assembly and synaptic transmission through its interaction with Daam1 and
392 Profilin (Wagh et al., 2015). Daam1 is a formin and a known regulator/interaction partner of Dvl1
393 (Gao and Chen, 2010). It is thus possible that, in the absence of Piccolo, Dvl1 is not properly
394 localized to presynaptic sites, preventing proper Wnt signaling and consequently causing the
395 formation of smaller and less organized MF-GC synapses. Furthermore, analysis of *Pclo*$^{gt/gt}$
396 transcripts reveals that Wnt expression is reduced (Medrano et al., 2019). Thus, there appears to
397 be at least two possible mechanisms that could contribute to smaller MF boutons in Piccolo
398 knockout rats: defects in SV recycling and Wnt signaling. Clearly further studies are needed to
399 explore these options.

400 A fundamental question raised by the anatomical, morphological and functional changes
401 within the cerebellum in rats lacking Piccolo is whether these changes affect the functionality of
402 the cerebellum. In behavioral tests, we observed that *Pclo*$^{gt/gt}$ rats performed significantly worse
403 than both *Pclo*$^{wt/wt}$ and *Pclo*$^{wt/gt}$ littermates at motor function tasks, highlighting the recessive
404 nature of the behavioral impairments. Our colleagues Medrano et al. (2019) also observed
405 epileptic seizures and increased aggression in *Pclo*$^{gt/gt}$ rats, and a failure to reproduce due to
406 impaired brain-gonad signaling.

407 Taken together, these data support the concept that Piccolo loss of function in patients
408 with PCH3 could be causal for many of the observed phenotypes, including changes in the
409 volume of brain structures and behavioral abnormalities such as impaired motor control and
410 epileptic seizures (Rajab et al., 2003; Namavar et al., 2011). With regard to reduced cerebellar
411 function, our studies highlight a prominent role for MF boutons which are not only smaller in size
412 but with altered synaptic properties. Mechanistic studies, which probe how Piccolo loss
413 contributes to these changes, should provide insights into the etiology of this devastating disease.
414

415 **Materials and Methods**

416 Generation of Piccolo KO rats (*Pclo*$^{gt/gt}$)

417 Generation of mutant Piccolo rat strains: Mutant rat strains harbored Sleeping Beauty β-Geo trap
418 transposons (Ivics et al., 2009), originally transmitted from a donor, recombinant rat
419 spermatogonial stem cell library (Izsvak et al., 2010). Recipient males were bred with wildtype
420 females to produce a random panel of mutant rat strains enriched with gene traps in protein
421 coding genes (Izsvak et al., 2010). All experiments were approved by the Institutional Animal
422 Care and Use Committee (IACUC) at UT-Southwestern Medical Center in Dallas, as certified by
423 the Association for Assessment and Accreditation of Laboratory Animal Care International
424 (AALAC) NIH OLAW Assurance # D16-00296.

425

426 Characterization of pups and genotyping

427 All procedures for experiments involving animals, were approved by the animal welfare
428 committee of Charité Medical University and the Berlin state government. P0-P2 rats were
429 weighed using Kern 440-43N scales and measured for approximate length with a ruler.
430 Genotyping of pups' cortices later revealed their genetic identity.

431 P0-P2 pups were genotyped using a PCR based reaction. In brief, brain tissue was
432 digested in lysis buffer (100 mM Tris-HCl (pH 8.0) with 10 mg/ml proteinase K, 100 mM NaCl)
433 for 5 minutes at 55 °C, before inhibiting Proteinase K by incubation at 99 °C for 10 minutes.
434 Samples were then centrifuged at 14,800 rpm for 2 minutes and 1 µl of supernatant was used for
435 the PCR reaction as outlined below.

436 For determination of genotype for adult rats, earpieces were taken and digested overnight
437 at 55 °C in SNET-buffer (400 mM NaCl, 1 % SDS, 200 mM Tris (pH 8.0), 5 mM EDTA)
438 containing 10 mg/ml proteinase K. Proteinase K enzyme reaction was stopped incubating the
439 samples for 10 min at 99 °C. The mixture was centrifuged for 2 min at 14,800 rpm. Supernatant
440 was transferred into a fresh tube and DNA was precipitated by addition of 100 % isopropanol.
441 Following samples were centrifuged for 15 min at 4 °C, 13,000 rpm. Precipitated DNA was

442 washed once with 70 % ethanol and centrifuged again for 5 min at 13,000 rpm. Supernatant was
443 discarded and the DNA pellet was air dried and resuspended in H2O. A PCR reaction with a
444 specific primer combination was performed on isolated DNA. The following primers were used:
445 Pclo KO F2: 3` gcaggaacacaaaccaacaa 5`; Pclo KO R1: 3` tgacctttagccggaactgt 5`; SBF2: 3`
446 tcatcaaggaaaccctggac 5`. The PCR reaction protocol was the following: 2 min 94 °C; 3 x (30 sec
447 94 °C, 60 °C 30 sec, 72 °C 30 sec); 35 x (94 °C 30 sec, 55 °C 30 sec, 72 °C 30 sec); 72 °C 10
448 min. Samples were mixed with a loading dye (New England BioLabs, MA, USA) and run on 2 %
449 agarose gel (Serva, Heidelberg, Germany) at 110 V for 45 min. The gel was imaged using
450 BioDocAnalyze UV transilluminator and BioDocAnalyze2.2 software.
451
452 Western blot analysis
453 Brains from P0 – P2 pups were lysed in Lysis buffer (50 mM Tris-HCl, 150 mM NaCl, 5 mM
454 EDTA, 1 % Triton X-100, 0.5 % Deoxycholate, protease inhibitor pH 7.5) and incubated on ice
455 for 5 min. Samples were centrifuged at 13,000 rpm for 10 min at 4 °C. Afterwards the
456 supernatant was transferred into a fresh tube and the protein concentration was determined using
457 a BCA protein assay kit (Thermo Fisher scientific, Waltham, Massachusetts, USA). The same
458 protein amounts for *Pclo*$^{wt/wt}$, *Pclo*$^{wt/gt}$ and *Pclo*$^{gt/gt}$ samples were separated by SDS-PAGE and
459 transferred onto nitrocellulose membranes (running buffer: 25 mM Tris, 190 mM Glycine, 0.1 %
460 SDS, pH 8.3; transfer buffer: 25 mM Tris, 192 mM Glycine, 1 % SDS, 10 % Methanol for small
461 proteins, 7 % Methanol for larger proteins pH 8.3). After the transfer, nitrocellulose membranes
462 were blocked with 5 % milk in TBST (20 mM Tris pH 7.5, 150 mM NaCl, 0.1 % Tween 20) and
463 incubated with primary antibodies in 3 % milk in TBST overnight at 4 °C. The following
464 antibodies were used: Piccolo (1:1000; rabbit; Synaptic Systems, Göttingen, Germany; Cat#
465 142002), $GABA_A\alpha6$ receptor (1:300; Merck Darmstadt, Germany; Cat# 06-868) overnight.
466 Nitrocellulose membranes were washed 3 times for 10 min with TBST and incubated with HRP-
467 conjugated secondary antibodies for 1 h at RT (1:1000; Sigma-Aldrich, St. Louis, USA; Cat#

468 NA9310 Cat# NA934). Membranes were washed 3 times for 10 min with TBST, afterwards
469 secondary antibody binding was detected with ECL Western Blotting Detection Reagents
470 (Thermo Fisher Scientific, Waltham, USA) and a Fusion FX7 image and analytics system (Vilber
471 Lourmat, Collégien, France).
472
473 Immunohistochemistry
474 Immunohistochemistry was performed on brain tissue from rats perfused with 4 %
475 paraformaldehyde (Roth, Karlsruhe, Germany) dissolved in PB (80 mM Na2HPO4 (Roth,
476 Karlsruhe, Germany), 20 mM NaH2PO4 (Bernd Kraft, Duisburg, Germany)) (PFA). Brains were
477 extracted and placed in 4 % PFA overnight, cryoprotected in 15 % and then 30 % sucrose
478 solution (Sigma-Aldrich, St. Louis, USA; dissolved in PB) for 24 hours each. Brains were snap-
479 frozen by submersion in 2-methylbutane (Roth, Karlsruhe, Germany) cooled to -60 °C and then
480 stored at -20 °C until use. Brains were cut para-sagittally or coronally with a Leica cryostat to
481 either 20 µm thick sections and mounted on superfrost slides (Thermo Fisher Scientific,
482 Waltham, USA), or 50 µm sections which were processed free-floating. Slides were left to dry for
483 a minimum of one hour before storage at -20 °C and free-float sections were stored in antifreeze
484 solution (30 % Ethylene glycol, 30 % Glycerol (Roth, Karlsruhe, Germany), 30 % ddH2O, 10 %
485 0.244M PO4 buffer (NaOH, NaH2PO4, Roth, Karlsruhe, Germany)).
486 Prior to staining at least 4 slides (each containing two sections) from each animal were
487 left to equilibrate at room temperature (RT) for one hour. Sections were selected to encompass
488 the range of the axis we were investigating. A hydrophobic barrier was created around sections
489 using a DAKO pen (DAKO, Glostrup, Denmark) and sections were washed and permeabilized
490 with TBS (20 mM Tris pH 7.5, 150 mM NaCl, Roth, Karlsruhe, Germany) with 0.025 % Triton
491 X-100 (Roth, Karlsruhe, Germany) (TBST) for 3 x 5 min, prior to blocking with 10 % Normal
492 Goat Serum (NGS, Sigma-Aldrich, St. Louis, USA) with 1 % Bovine Serum Albumin (BSA,
493 Sigma-Aldrich, St. Louis, USA) in TBS. The following primary antibodies were used: Calbindin

494 (1:750; rabbit; Synaptic Systems, Göttingen, Germany; Cat# 214002), $GABA_A$ receptor α subunit
495 (1:250; rabbit; Sigma-Aldrich, St. Louis, USA; Cat# G5544), MAP2 (1:1000; chicken;
496 MilliporeSigma, Burlington, USA, Cat# AB5543), Piccolo (1:200; guinea pig; Synaptic Systems,
497 Göttingen, Germany; Cat# 142 104), VGluT1 (1:1000; rabbit; Abcam, Cambridge, UK; Cat#
498 ab104898), VGluT2 (1:250; guinea pig; Synaptic Systems, Göttingen, Germany; Cat#
499 13540419). VGluT2 (1:300; mouse monoclonal (epitope AA 566 to 582); Synaptic Systems,
500 Göttingen, Germany; Cat# 135 421). Antibodies diluted in TBS with 1 % BSA were applied and
501 left overnight at 4 °C. After 3 x 5 min washing with TBST, differently labeled secondary
502 antibodies were used from Invitrogen (Thermo Fisher Scientific, Waltham, USA, dilution
503 1:1000), again diluted in 1 % BSA in TBS antibody solution and then applied for 1 hour at RT.
504 Sections were then washed with TBS 2 x 10 min or, if desired, incubated in TBS with DAPI
505 (Roth, Karlsruhe, Germany) for 30 min before washing again 2 x 10 min. Slides were
506 coverslipped (24x50 mm coverslips, Menzel Gläser, Braunschweig, Germany) with Immu-Mount
507 (Shandon-Thermo Scientific, Cheshire, UK) and sealed with clear nail polish once hardened.
508
509 Nissl stain
510 Sections were washed 3 times in PBS then mounted onto superfrost slides and allowed to dry for
511 1-2 days. Slides were inserted into slide racks and passed through the following solutions: 95 %
512 EtOH (Ethanol from Roth, Karlsruhe, Germany; diluted as appropriate with ddH2O) x 15 min, 70
513 % EtOH, 50 % EtOH, ddH2O, 10 min Blue counterstain (TACS from Trevigen, MD, USA),
514 ddH2O and then dehydrated through 50 %, 70 % acid EtOH (1 % glacial acetic acid (Th. Geyer,
515 Renningen, Germany) in 70 % EtOH), 95 % and 100 % EtOH before clearing in Roti Histol
516 (Roth, Karlsruhe, Germany), coverslipped using Entellan mounting medium (Entellan,
517 Darmstadt, Germany) and left to dry for 24 hours under a fume hood.
518
519 Confocal z-stack image acquisition and processing

520 Images were acquired on a spinning disc confocal microscope (Zeiss Axio Observer.Z1 with
521 Andor spinning disc and cobolt, omricron, i-beam laser) using a 40x (1.3 NA) and 100x (1.4 NA)
522 Plan-Apochromat oil objective and an iXon ultra (Andor, Belfast, UK) camera controlled by iQ
523 software (Andor, Belfast, UK). Sections for $GABA_A\alpha6$ analysis (Figure 7) were imaged with a
524 Nikon Spinning Disk Confocal CSU-X using a 100x (1.45 NA) Plan Apo oil objective and an
525 EMCCD camera with Andor Revolution SD System(Andor, Belfast, UK).
526
527 Tile scan overview images
528 An upright microscope (Olympus BX61) was used to image fluorescently stained cerebellar
529 sections. A CCD color camera was used with a 10x or 5x lens for overview pictures. CellSens
530 software (Olympus, Hamburg, Germany) stitched multiple images together to give an overview
531 of the whole cerebellar region.
532
533 Image analysis
534 For image processing and analysis ImageJ/FIJI software was used (Schindelin et al., 2012). For
535 analysis of $Pclo^{wt/wt}$ and $Pclo^{gt/gt}$ tissue sections were selected from the vermis and approximately
536 every 10th slide laterally (each slide containing 2 sections) was analyzed. The best quality section
537 per slide was imaged. For layer thickness, all lobes were measured and for closer analysis of MF
538 size, CF coverage and GC density, images were taken from lobes I, III, V, VII and IX where
539 possible. For $GABA_a\alpha6$ subunit expression, 6 images were taken per slide, 4 slides per animal.
540 Average signal intensity was measured for the whole field of view in the $GABA_a\alpha6$ antibody
541 channel and then normalized to the MAP2 channel for each image.
542 Layer 'thickness' was calculated per lobe by dividing the area of the layer by the inner
543 length of the layer for both GCL and ML. For Purkinje cell density, the number of PCs per lobe
544 was counted and divided by the length of the PC layer for that lobe. Data points represent
545 'thickness' values from individual lobes.

546 Granule cell density was calculated from 100x magnification single plane images stained
547 with DAPI. GCs were counted per image by an experimenter blinded to the genotype of each
548 image, and this number divided by the area of each image. Data points represent each image. .
549 Mossy fiber cluster size was measured using a script within ImageJ to analyze particles
550 stained with VGluT1 and/or VGluT2. The area of each puncta was measured and an average
551 taken per image. Data points represent average cluster size of each image.
552 Climbing fiber innervation was assessed using VGluT2 and Calbindin staining. The
553 molecular layer area was defined in the Calbindin channel, consisting of Calbindin-positive PC
554 dendrites, and the VGluT2 channel was selected and pasted into a new imageJ file. The same
555 script as for MF analysis was run to calculate the total area stained with VGluT2, divided by the
556 area of the ML and x100 to give percentage coverage. Data presented represent percentage per
557 image.
558
559 Electron microscopy
560 *Pclo*$^{wt/wt}$ and *Pclo*$^{gt/gt}$ rats were anesthetized deeply with 33 mg/ml Ketamine (Inresa Arzneimittel
561 GmbH, Freiburg, Germany) 830 µg/ml Xylavet (cp-pharma, Burgdorf, Germany) and perfused
562 transcardially with 37 °C physiological saline for 3 to 4 min followed by a 0.1 M phosphate
563 buffer containing 4 % paraformaldehyde and 0.05 % glutaraldehyde. Brains were stored in
564 fixative overnight and subsequently sliced sagittally (350 µm) on a vibratome. Regions of interest
565 were cut into small pieces and post-fixed in 1 % OsO4 and 0.1 M sodium cacodylate and en-bloc
566 stained in 1 % uranyl acetate aqueous solution. Finally, samples were dehydrated and embedded
567 in epoxy resin (Epon 812; EMS). Ultrathin sections were cut using an Ultracut ultramicrotome
568 (UCT, Leica, Wetzlar, Germany) equipped with a diamond knife (Ultra 45, DiATOME, Hatfield,
569 USA) and collected on formvar-coated 200-mesh copper grids (EMS). Sections were imaged in a
570 Zeiss EM-900 Transmission Electron Microscope (Zeiss) operated at 80 keV and equipped with a
571 2K x 2K CCD camera. Data were analyzed blindly using the ImageJ software. Data points

572 represent analysis from individual images obtained from 3 rats per genotype. For histological and
573 EM data, a normality test was performed (D'Agostino-Pearson omnibus normality test). If
574 successful then a student's t-test was used to compare *Pclo*$^{wt/wt}$ to *Pclo*$^{gt/gt}$ rats, or alternatively a
575 test for non-normal data (Mann-Whitney U test) was used.
576
577 Electrophysiology methods
578 Cerebellar slices were prepared from 3-to-4 month-old *Pclo*$^{wt/wt}$ and *Pclo*$^{gt/gt}$ rats of either sex.
579 Animals were treated in accordance with the German Protection of Animals Act and with the
580 guidelines for the welfare of experimental animals issued by the European Communities Council;
581 local authorities approved the experiments. Animals were anesthetized with isoflurane (Baxter,
582 Deerfield, IL) followed by a rapid decapitation with a custom-built guillotine. The cerebellar
583 vermis was quickly removed and mounted in a chamber filled with chilled extracellular solution.
584 Parasagittal 300 µm slices were cut using a Leica VT1200 microtome (Leica Microsystems,
585 Wetzlar, Germany), transferred to an incubation chamber at ~35 °C for 30 min and subsequently
586 stored at RT. Artificial cerebrospinal fluid (ACSF) was used for slice cutting, storage, and
587 experiments. ACSF contained: 125 mM NaCl, 25 mM NaHCO3, 2.5 mM KCl, 1.25 mM
588 NaH2PO4, 1.1 mM CaCl2, 1 mM MgCl2, 3 mM Glucose, 17 mM Sucrose (~310 mOsm, pH 7.3
589 when bubbled with Carbogen (5% O2/95% CO2)). Patch pipettes were pulled from borosilicate
590 glass (Science Products, Hofheim, Germany) using a DMZ Puller (Zeitz-Instruments,
591 Martinsried, Germany). Patch pipettes had open-tip resistances of 6–9 MΩ. The intracellular
592 solution contained: 150 mM K-gluconate, 10 mM NaCl, 10 mM K-HEPES, 3 mM Mg-ATP, 0.3
593 mM Na-GTP (300–305 mOsm, pH adjusted to 7.3 with KOH). In some of the experiments, the
594 intracellular solution contained 10 µM of the fluorescence dye Atto594. Experiments were
595 performed at 35–37 °C and slices were continuously superfused with ACSF containing 20 µM
596 SR95531 and 40 µM D-(2R)-amino-5-phosphonovaleric acid (D-APV) to block Golgi-cell

597 inhibition and NMDA-receptors, respectively. Atto594 was obtained from Atto-Tec (Atto-Tec,
598 Siegen, Germany); all other chemicals were purchased from Sigma-Aldrich (St. Louis, MO).
599
600 Current clamp recordings.
601 To determine the input resistance, subthreshold current pulses were applied from -20 to +20 pA
602 in 2pA steps. Action potentials were evoked in current-clamp mode by current pulses (amplitude
603 20-400 pA, duration 300 ms). The resistance of the solution-filled patch-pipettes was 24.9 ± 1
604 MΩ and 23 ± 1 MΩ for *Pclo*$^{wt/wt}$ and *Pclo*$^{gt/gt}$ rats respectively. Patch-clamp recordings were made
605 using a HEKA EPC10/2 USB amplifier (HEKA Elektronik, Lambrecht/Pfalz, Germany). Data
606 were sampled at 200 kHz. Measurements were corrected for a liquid junction potential of +16
607 mV.
608 Excitatory postsynaptic currents (EPSCs)
609 To measure evoked EPSCs, GCs were held at a holding potential of – 80 mV and Mossy fiber
610 axons were stimulated at 1 Hz. The stimulation voltage ranged between 16 to 40 V for control
611 and *Pclo*$^{gt/gt}$ animals. For spontaneous EPSCs GCs were held at -80 mV for around 3 minutes.
612 Single events were detected using the Igor Pro extension NeuroMatic (Rothman and Silver,
613 2018b) tool for Event detection.
614 The current clamp data were analyzed using custom-made procedures in Igor Pro
615 software (WaveMetrics, Oregon, USA) as described previously (PMID:31379501). In short,
616 properties of action potentials of GCs were determined from the injected currents, that elicited the
617 largest number of action potentials (APs). The action potential threshold was defined as the
618 membrane voltage at which the first derivative exceeded 100 V s^{-1}, the minimal AP peak was set
619 as -20 mV and the minimal amplitude to 20 mV. All APs with a half-width smaller than 50 µs
620 and higher than 500 µs were excluded. AP frequency and AP half-width were calculated from the
621 first three APs. Membrane capacitance, resting membrane potential and series resistance were
622 read from the amplifier software (HEKA) after achieving the whole-cell configuration. Input

623 resistance (R_{in}) was analyzed by plotting the steady-state voltage elicited by the subthreshold
624 current injections against the injected current and a spline interpolation was performed to obtain
625 the slope at the holding membrane potential (0 pA current injection).
626
627 **Excitatory postsynaptic currents**
628 To measure evoked EPSCs, GCs were held at a holding potential of – 80 mV and mossy fiber
629 axons were stimulated extracellular with a second patch pipette at 1 Hz. For spontaneous EPSCs
630 GCs, were held at -80 mV for around 3 minutes. Single events were detected using the template
631 detection algorithm of the Igor Pro extension NeuroMatic (Rothman and Silver, 2018a).
632
633 EPSCs were analyzed with the Igor Pro software. The amplitude and the kinetics were
634 determined from the average of 25 individual single EPSCs. To obtain the decay kinetics, single
635 EPSCs were fitted with one or two exponentials. The weighted time constant was calculated as:
636

$$\tau w = \frac{Aslow\ \tau slow\ +\ Afast\ \tau fast}{Aslow\ +\ Afast}$$

637
638 Behavioral assessment
639 Rotarod task
640 The apparatus (IITC Life Science, Woodland Hills, CA) consisted of 5 semi-enclosed lanes and
641 an elevated metal rod (9.525 cm diameter, 29.21 cm elevation) with a fine textured finish to
642 enhance grip. For each trial, all rats were placed on the unmoving rod, allowed to stabilize their
643 posture, and then rod rotation was initiated. Test parameters were: rotation direction, toward
644 investigator to encourage rats to face away while walking; start speed, 4 rpm; top speed, 44 rpm;
645 acceleration rate, 0.2 rpm/s (200 sec from start to top speed); max test duration, 300 s. Each rat's
646 trial ended when it fell from the rod, triggering the fall-detection sensor. Data was automatically

647 recorded to a computer. Rats underwent 4 trials/day, with an inter-trial interval of at least 10 min
648 for 4 consecutive days.
649
650 Ladder rung task
651 Ladder rung tests were performed on cohorts of *Pclo*$^{wt/wt}$, Pclo$^{wt/gt}$ and *Pclo*$^{gt/gt}$ rats by methods
652 previously described (Metz and Whishaw, 2009). Rats were trained to cross a plexiglass tunnel
653 about 1 m long with metal rods provided at regular intervals as steps. Each step that the rat took
654 was scored on the basis of paw placement on a 7 category scale with 0 being paw totally missing
655 the rung and 6 being correct paw placement. The average score per pair of limbs was used to
656 quantify step score. During the trial, the error per step was also quantified by number of low
657 scoring steps (0-2) divided by the total number of steps that the rat took during the test with each
658 pair of limbs (student's t-test). Data were derived from 3 trials with 3 cm rung separation
659 conducted on the same test day with at least a 10 min inter-trial interval, and group means were
660 compared using one-way ANOVA and Bonferroni post-hoc tests.
661
662 Grip test
663 To assess grip strength, rats were allowed to cling on to a support by forelimbs or hindlimbs and
664 pulled (Curzon et al., 2009). The support is attached to a transducer that can measure the pull
665 force being applied on the rat by the tester. During each trial, force that was necessary to be
666 applied by the tester to release the grip of the rat was recorded. Three trials per limb pair were
667 done and the means compared by student's t-test. To assess grip strength, the rat's torso was
668 supported ventrally while both forelimbs were allowed to grasp a metal support bar, then the rat
669 was pulled in a horizontal plane until the bar was released. Peak force was measured by a
670 transducer attached to the support bar (San Diego Instruments, San Diego, USA). Nine trials per
671 rat were conducted over two days (inter-trial interval at least 5 min) and group means were
672 compared using one-way ANOVA and Bonferroni post-hoc tests.

673

674 Open field test

675 The open field test (Curzon et al., 2009) was performed for each rat using a rectangular arena
676 (91.44 cm x 60.96 cm) divided into 9 equal sectors (1 center, 8 perimeter). At the start of the
677 experiment, the rat was placed in the center sector and allowed to explore for 10 min. The test
678 was recorded by digital video for later analysis. One test was conducted per rat. The behaviors
679 counted were crossing, rearing and grooming. Each crossing event was counted when all four
680 limbs of the test subject crossed the boundary of one sector into another. Rearing was defined as
681 the number of times the subject stood up on its hind limbs. Grooming was defined as the number
682 of times a rat licked or scratched itself while remaining stationary. Events that occurred in the
683 center versus perimeter sectors were tallied separately, and group means were analyzed for each
684 region by one-way ANOVA and Bonferroni post-hoc tests.

685

686 OptiMan system

687 Experiments were approved by the animal welfare committee of Charité Medical University and
688 the Berlin state government. Four groups (22 male & 4 female) of *Pclo*$^{wt/wt}$, Pclo$^{wt/gt}$ and *Pclo*$^{gt/gt}$
689 rats were used in this study. Rats carried subcutaneous radio-frequency identification (RFID) tags
690 in ventral location. Animals were group housed with 6 - 8 rats per group. Initially, all rats were
691 habituated to the OptiMan multi-cage environment with open sorter gates for voluntary
692 exploration. Then, automated sorting was activated so that only one rat could enter the operant
693 chamber at a time. During pull-task training, force thresholds and handle positions were adapted
694 every day for each session to the current skill level reached by a rat. Each session had 20 trials,
695 and two to three individual sessions were given per day with an intersession interval of 30 to 60
696 min. Within a session, the maximum time interval a rat was allowed to remain inactive between
697 trials was 6 - 8 min. A session ended when such inactivity occurred. The OptiMan (Operator
698 Independent Motor-Analysis, PhenoSys) system consists of two interconnected group home cages

699 (EU Type IV cage and 2000P) resting on an RFID sensor array plate that automatically tracks
700 RFID tag movement within the cage, and thus the locomotor activity of individual rats, day and
701 night. One of the home cages was connected via an electronic guillotine gate to a second cage
702 resting on a balance that automatically determined the body mass of a rat when inside this cage.
703 Individual animals voluntarily and self-motivated decided to visit the balance cage. Subsequent to
704 the balance cage, and again separated by an electronic guillotine gate, was a cage compartment
705 containing a horizontal ladder (1 m) with electronically monitored dual rungs on the left and right
706 side. From this ladder compartment, an animal entered a cage containing the isometric pull-task.
707 From there back to the home cage a rat passed over a force grid sensor array that sensed ground
708 forces exerted by the paws.
709
710 Isometric pull task
711 Rats were trained to pull a handle attached to a stationary force transducer with a predetermined
712 force threshold upon which they received a sugar pellet reward. Upon a rat's entry into the
713 isometric pull task cage a sugar pellet was delivered into the reward tray. A session started when
714 the rat retrieved this first reward, which led to the automatic closing of the entry gate, and to the
715 motorized slide-in appearance of the force handle to its predefined position. During each session,
716 5 different handle positions were presented to a rat. These positions varied from 11 mm inside the
717 cage wall (easiest position), to 7 mm outside of the cage wall (most difficult position). Handle
718 positions changed automatically during a session through a motorized slide. The difficulty level
719 within each handle position increased stepwise by increasing the force threshold for pellet release.
720 This started at 30 g pull-force and was increased to 40 g, 50 g and finally 60 g. A trial started
721 when a pull-force of 5 g was sensed. From then on, the pull-force was sampled for a duration of 4
722 sec. If a rat reached the force threshold within a 2 sec time interval then a trial was successful and
723 a reward delivered. The schedule then advanced to the next level of difficulty by either increasing
724 force threshold or moving the handle one position further towards the outside. Thus, a rat needed

725 a minimum of 20 trials to complete a session with 5 different handle positions and 4 different
726 force thresholds at each position. If the threshold was not reached then a trial was considered
727 unsuccessful and the rat had to continue with its next trial with unchanged conditions.
728 Experiments lasted for 15 experimental days with 2 - 3 daily sessions per individual.
729
730 Animal welfare
731 All animals were treated and cared for in accordance with national and institutional guidelines:
732 Generation of mutant Piccolo rat strains and behavioral experiments Figure 10 a-e: Rat
733 protocols were approved by the Institutional Animal Care and Use Committee (IACUC) at UT-
734 Southwestern Medical Center in Dallas, as certified by the Association for Assessment and
735 Accreditation of Laboratory Animal Care International (AALAC), permit number: NIH OLAW
736 Assurance # D16-00296.
737 Western blotting, immunohistochemistry, electron microscopy and behavioral
738 experiments with Optiman setup (Figure 10 d and e): Animals were treated in accordance with
739 the German Protection of Animals Act (TierSchG §4 Abs. 3); all procedures for experiments
740 involving animals were approved by the animal welfare committee of Charité Medical University
741 and the Berlin state government, permit number: T 0036/14.
742 Electrophysiology: Animals were treated in accordance with the German Protection of Animals
743 Act (TierSchG §4 Abs. 3) and with the guidelines for the welfare of experimental animals issued
744 by the European Communities Council Directive of 24. November 1986 (86/609/EEC). The local
745 authorities approved the experiments (Landesdirektion Leipzig), permit number: T24/18
746
747 Experimental design and statistical analysis
748 GraphPad Prism (RRID:SCR_002798) was used to analyze and represent data. Statistical design,
749 sample sizes and tests for each experiment can be found in the figure legends.
750

751 **References**

752 Ackermann F, Schink KO, Bruns C, Izsvak Z, Hamra FK, Rosenmund C, Garner CC (2019)
753 Critical role for Piccolo in synaptic vesicle retrieval. Elife 8.
754 Ahmad-Annuar A, Ciani L, Simeonidis I, Herreros J, Fredj NB, Rosso SB, Hall A, Brickley S,
755 Salinas PC (2006) Signaling across the synapse: a role for Wnt and Dishevelled in
756 presynaptic assembly and neurotransmitter release. J Cell Biol 174:127-139.
757 Ahmed MY, Chioza BA, Rajab A, Schmitz-Abe K, Al-Khayat A, Al-Turki S, Baple EL, Patton
758 MA, Al-Memar AY, Hurles ME, Partlow JN, Hill RS, Evrony GD, Servattalab S,
759 Markianos K, Walsh CA, Crosby AH, Mochida GH (2015) Loss of PCLO function
760 underlies pontocerebellar hypoplasia type III. Neurology 84:1745-1750.
761 Apps R, Garwicz M (2005) Anatomical and physiological foundations of cerebellar information
762 processing. Nat Rev Neurosci 6:297-311.
763 Brickley SG, Cull-Candy SG, Farrant M (1996) Development of a tonic form of synaptic
764 inhibition in rat cerebellar granule cells resulting from persistent activation of GABAA
765 receptors. J Physiol 497 (Pt 3):753-759.
766 Byczkowicz N, Ritzau-Jost A, Delvendahl I, Hallermann S (2018) How to maintain active zone
767 integrity during high-frequency transmission. Neurosci Res 127:61-69.
768 Cases-Langhoff C, Voss B, Garner AM, Appeltauer U, Takei K, Kindler S, Veh RW, De Camilli
769 P, Gundelfinger ED, Garner CC (1996) Piccolo, a novel 420 kDa protein associated with
770 the presynaptic cytomatrix. Eur J Cell Biol 69:214-223.
771 Chen AI, Zang K, Masliah E, Reichardt LF (2016) Glutamatergic axon-derived BDNF controls
772 GABAergic synaptic differentiation in the cerebellum. Sci Rep 6:20201.
773 Curzon P, Zhang M, Radek RJ, Fox GB (2009) The Behavioral Assessment of Sensorimotor
774 Processes in the Mouse: Acoustic Startle, Sensory Gating, Locomotor Activity, Rotarod,
775 and Beam Walking. In: Methods of Behavior Analysis in Neuroscience (nd, Buccafusco
776 JJ, eds). Boca Raton (FL).
777 Durmaz B, Wollnik B, Cogulu O, Li Y, Tekgul H, Hazan F, Ozkinay F (2009) Pontocerebellar
778 hypoplasia type III (CLAM): Extended phenotype and novel molecular findings. J Neurol
779 256:416-419.
780 Eccles JC, Llinás R, Sasaki K (1966) The mossy fibre-granule cell relay of the cerebellum and its
781 inhibitory control by Golgi cells. Experimental Brain Research 1:82-101.
782 Fenster SD, Garner CC (2002) Gene structure and genetic localization of the PCLO gene
783 encoding the presynaptic active zone protein Piccolo. Int J Dev Neurosci 20:161-171.
784 Fenster SD, Chung WJ, Zhai R, Cases-Langhoff C, Voss B, Garner AM, Kaempf U, Kindler S,
785 Gundelfinger ED, Garner CC (2000) Piccolo, a presynaptic zinc finger protein
786 structurally related to bassoon. Neuron 25:203-214.
787 Gao C, Chen YG (2010) Dishevelled: The hub of Wnt signaling. Cell Signal 22:717-727.
788 Gundelfinger ED, Reissner C, Garner CC (2015) Role of Bassoon and Piccolo in Assembly and
789 Molecular Organization of the Active Zone. Front Synaptic Neurosci 7:19.
790 Hall AC, Lucas FR, Salinas PC (2000) Axonal remodeling and synaptic differentiation in the
791 cerebellum is regulated by WNT-7a signaling. Cell 100:525-535.
792 Hashimoto K, Kano M (1998) Presynaptic origin of paired-pulse depression at climbing fibre-
793 Purkinje cell synapses in the rat cerebellum. J Physiol 506 (Pt 2):391-405.
794 Hashimoto K, Ichikawa R, Kitamura K, Watanabe M, Kano M (2009) Translocation of a
795 "winner" climbing fiber to the Purkinje cell dendrite and subsequent elimination of
796 "losers" from the soma in developing cerebellum. Neuron 63:106-118.
797 Heyden A, Ionescu MCS, Romorini S, Kracht B, Ghiglieri V, Calabresi P, Seidenbecher C,
798 Angenstein F, Gundelfinger ED (2011) Hippocampal enlargement in Bassoon-mutant
799 mice is associated with enhanced neurogenesis, reduced apoptosis, and abnormal BDNF
800 levels. Cell Tissue Res 346:11-26.

801 Homanics GE, Ferguson C, Quinlan JJ, Daggett J, Snyder K, Lagenaur C, Mi Z-P, Wang X-H,
802 Grayson DR, Firestone LL (1997) Gene Knockout of the α6 Subunit of the γ-
803 Aminobutyric Acid Type A Receptor: Lack of Effect on Responses to Ethanol,
804 Pentobarbital, and General Anesthetics. Molecular Pharmacology 51:588-596.
805 Hubler D, Rankovic M, Richter K, Lazarevic V, Altrock WD, Fischer KD, Gundelfinger ED,
806 Fejtova A (2012) Differential spatial expression and subcellular localization of CtBP
807 family members in rodent brain. PLoS One 7:e39710.
808 Human Protein Atlas (2015) PCLO. In.
809 Ichikawa R, Hashimoto K, Miyazaki T, Uchigashima M, Yamasaki M, Aiba A, Kano M,
810 Watanabe M (2016) Territories of heterologous inputs onto Purkinje cell dendrites are
811 segregated by mGluR1-dependent parallel fiber synapse elimination. Proc Natl Acad Sci
812 U S A 113:2282-2287.
813 Ivanova D, Dirks A, Montenegro-Venegas C, Schone C, Altrock WD, Marini C, Frischknecht R,
814 Schanze D, Zenker M, Gundelfinger ED, Fejtova A (2015) Synaptic activity controls
815 localization and function of CtBP1 via binding to Bassoon and Piccolo. EMBO J
816 34:1056-1077.
817 Ivics Z, Li MA, Mates L, Boeke JD, Nagy A, Bradley A, Izsvak Z (2009) Transposon-mediated
818 genome manipulation in vertebrates (vol 6, pg 415, 2009). Nat Methods 6:546-546.
819 Izsvak Z, Frohlich J, Grabundzija I, Shirley JR, Powell HM, Chapman KM, Ivics Z, Hamra FK
820 (2010) Generating knockout rats by transposon mutagenesis in spermatogonial stem cells.
821 Nat Methods 7:443-445.
822 Jakab RL, Hamori J (1988) Quantitative Morphology and Synaptology of Cerebellar Glomeruli in
823 the Rat. Anat Embryol 179:81-88.
824 Leto K et al. (2016) Consensus Paper: Cerebellar Development. Cerebellum 15:789-828.
825 Maex R, De Schutter E (1998) Synchronization of golgi and granule cell firing in a detailed
826 network model of the cerebellar granule cell layer. J Neurophysiol 80:2521-2537.
827 Maricich SM, Aqeeb KA, Moayedi Y, Mathes EL, Patel MS, Chitayat D, Lyon G, Leroy JG,
828 Zoghbi HY (2011) Pontocerebellar Hypoplasia: Review of Classification and Genetics,
829 and Exclusion of Several Genes Known to Be Important for Cerebellar Development.
830 Journal of Child Neurology 26:288-294.
831 Medrano GA, Singh M, Plautz EJ, Good LB, Chapman KM, Chaudhary J, Jaichander P, Powell
832 HM, Pudasaini A, Shelton JM, Richardson JA, Xie X-J, Ivics Z, Braun C, Ackermann F,
833 Garner CC, Izsvák Z, Hamra FK (2019) Mutant screen reveals depression-associated
834 *Piccolo's* control over brain-gonad cross talk and reproductive behavior.
835 bioRxiv:405985.
836 Metz GA, Whishaw IQ (2009) The ladder rung walking task: a scoring system and its practical
837 application. J Vis Exp.
838 Miyashita S, Adachi T, Yamashita M, Sota T, Hoshino M (2017) Dynamics of the cell division
839 orientation of granule cell precursors during cerebellar development. Mech Dev 147:1-7.
840 Miyazaki T, Fukaya M, Shimizu H, Watanabe M (2003) Subtype switching of vesicular
841 glutamate transporters at parallel fibre-Purkinje cell synapses in developing mouse
842 cerebellum. Eur J Neurosci 17:2563-2572.
843 Muller TM, Gierke K, Joachimsthaler A, Sticht H, Izsvak Z, Hamra FK, Fejtova A, Ackermann
844 F, Garner CC, Kremers J, Brandstatter JH, Regus-Leidig H (2019) A Multiple Piccolino-
845 RIBEYE Interaction Supports Plate-Shaped Synaptic Ribbons in Retinal Neurons. J
846 Neurosci 39:2606-2619.
847 Namavar Y et al. (2011) Clinical, neuroradiological and genetic findings in pontocerebellar
848 hypoplasia. Brain 134:143-156.
849 Nusser Z, Sieghart W, Somogyi P (1998) Segregation of different GABAA receptors to synaptic
850 and extrasynaptic membranes of cerebellar granule cells. J Neurosci 18:1693-1703.

Nusser Z, Sieghart W, Stephenson F, Somogyi P (1996) The alpha 6 subunit of the GABAA receptor is concentrated in both inhibitory and excitatory synapses on cerebellar granule cells. The Journal of Neuroscience 16:103-114.

Rajab A, Mochida GH, Hill A, Ganesh V, Bodell A, Riaz A, Grant PE, Shugart YY, Walsh CA (2003) A novel form of pontocerebellar hypoplasia maps to chromosome 7q11-21. Neurology 60:1664-1667.

Regus-Leidig H, Fuchs M, Lohner M, Leist SR, Leal-Ortiz S, Chiodo VA, Hauswirth WW, Garner CC, Brandstatter JH (2014) In vivo knockdown of Piccolino disrupts presynaptic ribbon morphology in mouse photoreceptor synapses. Front Cell Neurosci 8:259.

Rothman JS, Silver RA (2018a) NeuroMatic: An Integrated Open-Source Software Toolkit for Acquisition, Analysis and Simulation of Electrophysiological Data. Front Neuroinform 12:14.

Rothman JS, Silver RA (2018b) NeuroMatic: An Integrated Open-Source Software Toolkit for Acquisition, Analysis and Simulation of Electrophysiological Data. Front Neuroinform 12.

Rudnik-Schoneborn S, Barth PG, Zerres K (2014) Pontocerebellar hypoplasia. Am J Med Genet C Semin Med Genet 166C:173-183.

Salinas PC, Zou YM (2008) Wnt signaling in neural circuit assembly. Annual Review of Neuroscience 31:339-358.

Scheiffele P (2003) Cell-cell signaling during synapse formation in the CNS. Annual Review of Neuroscience 26:485-508.

Schindelin J, Arganda-Carreras I, Frise E, Kaynig V, Longair M, Pietzsch T, Preibisch S, Rueden C, Saalfeld S, Schmid B, Tinevez JY, White DJ, Hartenstein V, Eliceiri K, Tomancak P, Cardona A (2012) Fiji: an open-source platform for biological-image analysis. Nat Methods 9:676-682.

Shinoda Y, Sugiuchi Y, Futami T, Izawa R (1992) Axon Collaterals of Mossy Fibers from the Pontine Nucleus in the Cerebellar Dentate Nucleus. Journal of Neurophysiology 67:547-560.

Sillitoe R, Fu, Y., Watson, C. (2012) Chapter 11 - Cerebellum: Academic Press.

Solecki DJ, Liu XL, Tomoda T, Fang Y, Hatten ME (2001) Activated Notch2 signaling inhibits differentiation of cerebellar granule neuron precursors by maintaining proliferation. Neuron 31:557-568.

Turrigiano G (2012) Homeostatic synaptic plasticity: local and global mechanisms for stabilizing neuronal function. Cold Spring Harb Perspect Biol 4:a005736.

Voogd J, Glickstein M (1998) The anatomy of the cerebellum. Trends Neurosci 21:370-375.

Wagh D, Terry-Lorenzo R, Waites CL, Leal-Ortiz SA, Maas C, Reimer RJ, Garner CC (2015) Piccolo Directs Activity Dependent F-Actin Assembly from Presynaptic Active Zones via Daam1. PLoS One 10:e0120093.

Waites CL, Craig AM, Garner CC (2005) Mechanisms of vertebrate synaptogenesis. Annual Review of Neuroscience 28:251-274.

Waites CL, Leal-Ortiz SA, Okerlund N, Dalke H, Fejtova A, Altrock WD, Gundelfinger ED, Garner CC (2013) Bassoon and Piccolo maintain synapse integrity by regulating protein ubiquitination and degradation. EMBO J 32:954-969.

Wallace VA (1999) Purkinje-cell-derived Sonic hedgehog regulates granule neuron precursor cell proliferation in the developing mouse cerebellum. Curr Biol 9:445-448.

Xu-Friedman MA, Regehr WG (2003) Ultrastructural contributions to desensitization at cerebellar mossy fiber to granule cell synapses. Journal of Neuroscience 23:2182-2192.

Zelnik N, Dobyns WB, Forem SL, Kolodny EH (1996) Congenital pontocerebellar atrophy in three patients: clinical, radiologic and etiologic considerations. Neuroradiology 38:684-687.

Zhai RG, Vardinon-Friedman H, Cases-Langhoff C, Becker B, Gundelfinger ED, Ziv NE, Garner CC (2001) Assembling the presynaptic active zone: a characterization of an active one precursor vesicle. Neuron 29:131-143.

906 **Figure Legends**

907

908 **Figure 1.** Generation of *Pclo*$^{gt/gt}$ mutant animals.

909 A) Sleeping beauty transposon mutagenesis was used to generate gene trap (gt) piccolo knockout
910 rats. The transposon element inserted into exon 3 of the piccolo genomic sequence and caused a
911 stop in the reading frame. Adapted from Ackermann et al. (Ackermann et al., 2019).

912 B) Pairs of heterozygous (*Pclo*$^{wt/gt}$) males and females produced litters with Mendelian
913 distribution. Pie chart demonstrates the birth rates of homozygous wildtype (*Pclo*$^{wt/wt}$),
914 homozygous gene trap mutation (*Pclo*$^{gt/gt}$) and heterozygous (*Pclo*$^{wt/gt}$) pups.

915 C) Western blot analysis of brain lysates prepared from postnatal day 2 (P2) animals to confirm
916 the loss of full-length Piccolo protein from the brain. A band of the Piccolo-corresponding size of
917 560 kDa is detectable in lysates prepared from *Pclo*$^{wt/wt}$ and *Pclo*$^{wt/gt}$ animals, but is absent in
918 *Pclo*$^{gt/gt}$ brain lysates (data are representative of 3 independent experiments). However, smaller
919 bands between 100 and 70 kDA are still present in *Pclo*$^{gt/gt}$ brain lysates.

920 D-F) Image of postnatal day 1 (P1) littermates (D), E) Quantification of the body length of P0-P2
921 *Pclo*$^{wt/wt}$ and *Pclo*$^{gt/gt}$ pups (*Pclo*$^{wt/wt}$ = 5.5 cm ± 0.077, n = 23; *Pclo*$^{gt/gt}$ = 5.15 cm ± 0.070, n = 27; 6
922 independent litters; unpaired t-test, $p^{**} = 0.0014$). F) Quantification of the body weight of P0-P2
923 *Pclo*$^{wt/wt}$ and *Pclo*$^{gt/gt}$ pups (*Pclo*$^{wt/wt}$ = 8.09 g ± 0.203, n = 39; *Pclo*$^{gt/gt}$ = 7.31 g ± 0.166, n = 35; 12
924 independent litters; unpaired t-test, $p^{**} = 0.0044$).

925 G-H) Image of brains dissected from P1 *Pclo*$^{wt/wt}$ and *Pclo*$^{gt/gt}$ pups (G). H) Quantification of the
926 brain weight of P0-P2 *Pclo*$^{wt/wt}$ and *Pclo*$^{gt/gt}$ pups (*Pclo*$^{wt/wt}$ = 0.293 ± 0.00533, n = 7;
927 *Pclo*$^{gt/gt}$ = 0.289 g ± 0.00758 n = 3; 3 independent litters; unpaired t-test, $p = 0.683$)

928 I) Nissl stained sagittal sections from P2 rat brains show no overt differences between *Pclo*$^{gt/gt}$
929 and *Pclo*$^{wt/wt}$ pups. Scale bar = 0.5 cm.

930 J-L) Image of 4% PFA-perfused brains from *Pclo*$^{wt/wt}$ and *Pclo*$^{gt/gt}$ animals at 3 months of age (I),
931 K) Quantification of the brain weight showing that *Pclo*$^{gt/gt}$ brains are significantly lighter than

932 *Pclo*$^{wt/wt}$ brains (*Pclo*$^{wt/wt}$ = 2.098 g ± 0.074, *Pclo*$^{gt/gt}$ = 1.435 g ± 0.021; n = 6, Mann-Whitney U
933 test, $p^{**} = 0.0022$).
934 L) Nissl stained sagittal sections from 3 month-old rat brains reveal microcephaly in *Pclo*$^{gt/gt}$
935 compared to *Pclo*$^{wt/wt}$. Note, ventricles are larger and cerebellum, pons, cerebrum and subcortical
936 regions are smaller.
937 Scale bars: 1 cm (G and K); 0.5 cm (I). Error bars represent SEM.
938
939 **Figure 2.** *Pclo*$^{gt/gt}$ rats show cortical thinning and a smaller pons area compared to *Pclo*$^{wt/wt}$
940 littermates.
941 A-B) Nissl stained somatosensory cortex (indicated by dashed lines) (A) and the brainstem
942 including pontine area (B) of *Pclo*$^{wt/wt}$ and *Pclo*$^{gt/gt}$ brains at 3 month of age. B) Zoom
943 demonstrates that pontine neurons are of similar density in *Pclo*$^{wt/wt}$ and *Pclo*$^{gt/gt}$.
944 C) Pontine area visualized by staining with antibodies against VGluT1 and subsequent DAB
945 conversion of *Pclo*$^{wt/wt}$ and *Pclo*$^{gt/gt}$ brains at 3 month of age.
946 D) Quantification of the thickness of the somatosensory cortex (*Pclo*$^{wt/wt}$ = 2.18 mm ± 0.045, n =
947 25 brain sections; *Pclo*$^{gt/gt}$ = 1.98 mm ± 0.041, n = 21 brain sections; n = 3 independent
948 experiments; unpaired t-test, $p^{**} = 0.0018$).
949 E) Quantification of the area of the pons (*Pclo*$^{wt/wt}$ = 12.24 mm^2 ± 0.620, n = 26 brain sections;
950 *Pclo*$^{gt/gt}$ = 5.58 mm^2 ± 0.333, n = 17 brain sections; n = 3 independent experiments; unpaired t-
951 test, $p^{****} < 0.0001$).
952 Scale bars: 200 µm (A and C), 500 µm (B and C) and 100 µm (B, zoom). Error bars represent
953 SEM.
954
955 **Figure 3.** Morphometric comparison of *Pclo*$^{gt/gt}$ and *Pclo*$^{wt/wt}$ cerebella.
956 A-D) Images of sagittal sections of *Pclo*$^{wt/wt}$ and *Pclo*$^{gt/gt}$ cerebella at 3 month of age. The densely
957 packed granule cell layer (GCL) is visualized by DAPI staining. B) Higher magnification images

958 of (A) demonstrating GC density in the GCL. C) Quantification of the GCL thickness (*Pclo*$^{wt/wt}$ =
959 200.8 µm ± 2.932, n = 160 lobes; *Pclo*$^{gt/gt}$ = 134.8 µm ± 2.859, n = 148 lobes; n = 4 independent
960 experiments; Mann-Whitney U test, p**** <0.0001). D) Quantification of the number of GCs per
961 100 µm^2 (*Pclo*$^{wt/wt}$ = 1.702 ± 0.020, n = 111 images; *Pclo*$^{gt/gt}$ = 1.156 ± 0.022, n = 114 images; n =
962 3 independent experiments; unpaired t-test, p** = 0.0042).
963 E-H) Images of sagittal sections of *Pclo*$^{wt/wt}$ and *Pclo*$^{gt/gt}$ cerebella at 3 months of age. Purkinje
964 cells (PCs) stained with antibodies against Calbindin determine the molecular layer (ML) (lobes
965 I-III shown). F) Higher magnification images of (E). Note the closer packing of PCs in *Pclo*$^{gt/gt}$
966 compared to *Pclo*$^{wt/wt}$. G) Quantification of the ML thickness (*Pclo*$^{wt/wt}$ = 187.2 µm ± 2.719, n =
967 148 lobes; *Pclo*$^{gt/gt}$ = 127.2 µm ± 2.378, n = 125 lobes; n = 4 independent experiments; Mann-
968 Whitney U test, p**** < 0.0001). H) Quantification of the number of PCs per 100 µm length of
969 PC layer (*Pclo*$^{wt/wt}$ = 1.797 ± 0.036; n = 89 lobes; *Pclo*$^{gt/gt}$ = 2.554 ± 0.058; n = 65 lobes; n = 3
970 independent experiments; unpaired t-test, p**** < 0.0001).
971 I) Images of sagittal sections stained with antibodies against Calbindin showing that PCs migrate
972 correctly to their position in the ML and are correctly orientated.
973 Scale bars: 1cm (A), 20 µm (B and J), 50 µm (I) and 200 µm (F). Error bars represent SEM. Data
974 points represent images taken from lobes I, III, V, VII and IX; 4 sections per animal (B and D).
975
976 **Figure 4.** Abberant climbing fiber innervation of Purkinje cells in *Pclo*$^{gt/gt}$ rats compared to
977 *Pclo*$^{wt/wt}$ littermates.
978 A and B) Images of sagittal sections of *Pclo*$^{wt/wt}$ and *Pclo*$^{gt/gt}$ cerebella at 3 months of age stained
979 with antibodies against VGluT1 and Piccolo demonstrate the loss of Piccolo in the ML (A) and
980 the GCL (B) in *Pclo*$^{gt/gt}$ rats.
981 C) Images of sagittal sections of *Pclo*$^{wt/wt}$ and *Pclo*$^{gt/gt}$ cerebella at 3 months of age stained with
982 antibodies against Calbindin and VGluT2. Note that the climbing fiber synapses, immuno-
983 positive for VGluT2, are increased in the ML of *Pclo*$^{gt/gt}$ cerebella compared to *Pclo*$^{wt/wt}$ controls

984 (C and D). When Piccolo is absent, parallel fiber synapses in the ML - immuno-positive for
985 VGluT1 – do not appear overtly different between *Pclo*$^{wt/wt}$ and *Pclo*$^{gt/gt}$ (A). However, MF and CF
986 synapses are altered (4B-D, Figure 5).
987 D) Quantification of the percentage of the ML (indicated by dashed lines) immuno-positive for
988 VGluT2 from (C) (*Pclo*$^{wt/wt}$ = 3.521 ± 0.160, n = 128 images; *Pclo*$^{gt/gt}$ = 4.377 ± 0.241, n = 112
989 images; n = 3 independent experiments; Mann-Whitney U test, $p^* = 0.0278$).
990 Scale bars: 20 μm. Error bars represent SEM. Data points represent images taken from lobes I,
991 III, V, VII and IX; 4 sections per animal.
992
993 **Figure 5.** Cerebella from *Pclo*$^{gt/gt}$ animals have smaller mossy fiber rosettes.
994 A and B) Images of sagittal sections of *Pclo*$^{wt/wt}$ and *Pclo*$^{gt/gt}$ cerebella at 3 month of age stained
995 with antibodies against VGluT2, which is highly expressed at mossy fiber (MF) boutons, and the
996 somatodendritic marker MAP2 (A) or VGluT2 and VGluT1 (B). A) GCs extend their dendrites
997 into MF boutons in the *Pclo*$^{wt/wt}$ condition. However, in *Pclo*$^{gt/gt}$, whilst GC dendrites are still
998 juxtaposed to VGluT2-positive boutons, the boutons are smaller and therefore the arrangement is
999 less organized. B) Presynaptic MF glomeruli from lobes I (upper panel) and VII (lower panel) are
1000 visualized by VGluT1 and VGluT2. Note that the reduction in MF size is consistent regardless of
1001 the lobe. Note also that rosettes are generally labeled with either VGluT1 or VGluT2 and
1002 occasionally with both markers consistent with them being innervated by a single synaptic input
1003 from different neuronal cell types.
1004 C) Quantification of the size of VGluT1/VGluT2 clusters (*Pclo*$^{wt/wt}$ = 22.73 μm^2 ± 0.896, n = 4
1005 animals; *Pclo*$^{gt/gt}$ = 9.46 μm^2 ± 0.2899, n = 4 animals; unpaired t-test, $p^{****} < 0.0001$).
1006 D-E) Histograms to show the distribution of puncta sized 5-50 μm^2 (D) and 50-260 μm^2 (E). The
1007 shift of the data indicates *Pclo*$^{gt/gt}$ MFs have more smaller puncta (5 μm^2), whereas *Pclo*$^{wt/wt}$ MFs
1008 have more larger puncta (up to 260 μm^2).

1009 Scale bars: 50 µm (A and B) and 20 µm (B, zoom). Error bars represent SEM. Data points
1010 represent average puncta size per animal from images taken from lobes I, III, V, VII and IX, 4
1011 sections per animal (C, D and E).
1012
1013 **Figure 6.** $GABA_A$α6 subunit expression is lower in *Pclo*$^{gt/gt}$ than in *Pclo*$^{wt/wt}$.
1014 A) Representative images of sagittal sections of *Pclo*$^{wt/wt}$ and *Pclo*$^{gt/gt}$ cerebella at 3 months of age
1015 stained with antibodies against the $GABA_A$ subunit α6,VGluT2 and MAP2. Note the decreased
1016 levels of $GABA_A$α6 in the GC layer of *Pclo*$^{gt/gt}$ animals compared to *Pclo*$^{wt/wt}$ controls, quantified
1017 in B).
1018 B) Quantification of $GABA_A$ subunit α6, measured by the average intensity of antibody staining
1019 in images taken from the GC of the cerebellum, normalized to MAP2 antibody intensities for the
1020 same image (*Pclo*$^{wt/wt}$ = 0.661 ± 0.0479 arbitrary units (a.u.), n = 45 images from 3 individual
1021 animals; *Pclo*$^{gt/gt}$ = 0.443 ± 0.26 a.u., n = 44 images from 3 individual animals; Mann-Whitney U
1022 test, p^{***} = 0.0009).
1023 Scale bars: 20 µm. Error bars represent SEM. Data points represent images taken from 4 sections
1024 per animal.
1025
1026 **Figure 7.** Glomerular rosettes are smaller and less complex in *Pclo*$^{gt/gt}$.
1027 A, B and G) Electron microscopy images of the GCL of *Pclo*$^{wt/wt}$ and *Pclo*$^{gt/gt}$ cerebella at 3
1028 months of age. Granule cells are indicated by 'gc' (A and B), cerebellar glomeruli are highlighted
1029 in blue (*Pclo*$^{wt/wt}$) and green (*Pclo*$^{gt/gt}$) (A) and the presynaptic terminals of cerebellar MF are
1030 highlighted in blue (*Pclo*$^{wt/wt}$) and green (*Pclo*$^{gt/gt}$) (B). Asterisks mark active zones (AZs) (B) and
1031 the zoom in (G) emphasizes the presence of more clathrin-coated vesicles (CCVs) in *Pclo*$^{gt/gt}$ MF
1032 boutons compared to than *Pclo*$^{wt/wt}$.
1033 (C-F) Quantification of the size of glomeruli (C), the size of the MF presynapse (D), the
1034 complexity (squared perimeter/presynaptic area) of the MF bouton (E) and the density of AZs

1035 (F). Note the strong decrease in glomerulus and MF bouton size (C and D) (C) (*Pclo*$^{wt/wt}$ = 34.59
1036 μm^2 ± 1.287, n = 130 images; *Pclo*$^{gt/gt}$ = 18.82 μm^2 ± 0.853, n = 103 images; n = 3 independent
1037 experiments; Mann-Whitney U test, *p***** < 0.0001. (D) (*Pclo*$^{wt/wt}$ = 17.73 μm^2 ± 0.603, n = 141
1038 images; *Pclo*$^{gt/gt}$ = 11.69 μm^2 ± 0.497, n = 95 images; n = 3 independent experiments; Mann-
1039 Whitney U test, *p***** < 0.0001). (E) (*Pclo*$^{wt/wt}$ = 90.5 ± 4.089, n = 141 images; *Pclo*$^{gt/gt}$ = 58.1 ±
1040 3.818, n = 84 images; n = 3 independent experiments; Mann-Whitney U test, *p***** < 0.0001).
1041 (F) (*Pclo*$^{wt/wt}$ = 0.625 ± 0.021, n = 121 images; *Pclo*$^{gt/gt}$ = 0.652 ± 0.032, n = 84 images; n = 3
1042 independent experiments; Mann-Whitney U test, *p* = 0.7390).
1043 Scale bars: 2.5 μm (A), 1μm (B), 500 nm (G) and 250 nm (G, zoom). Error bars represent SEM.
1044
1045 **Figure 8.** Physiological assessment of mossy fiber boutons.
1046 A) Example Two-photon image of a cerebellar granule cell (GC) from a *Pclo*$^{gt/gt}$ rat filled with
1047 ATTO dye.
1048 B) Average data of biophysical properties of GCs for *Pclo*$^{wt/wt}$ and *Pclo*$^{gt/gt}$ rats. The input
1049 resistance of GCs was higher in *Pclo*$^{gt/gt}$ compared to *Pclo*$^{wt/wt}$ (Pclowt/wt = 722.6 MΩ ± 76.24, n
1050 = 22 cells; *Pclo*$^{gt/gt}$ = 1160 MΩ ± 154.9, n = 23 cells; n = 3 rats per genotype; Mann-Whitney U
1051 test, *p** = 0.0462). Whereas no differences were found in capacitance (*Pclo*$^{wt/wt}$ = 3.717 pF ±
1052 0.269, n = 21 cells; *Pclo*$^{gt/gt}$ = 3.643 pF ± 0.231, n = 23 cells; n = 3 rats per genotype; Mann-
1053 Whitney U test, *p* = 0.912), resting membrane potential (Vm) (*Pclo*$^{wt/wt}$ = -99.96 mV ± 1.261, n =
1054 18 cells, *Pclo*$^{gt/gt}$ = -100.8 mV ± 0.786, n = 23 cells; n = 3 rats per genotype; Mann-Whitney U
1055 test, *p* = 0.612), the half-duration of the action potential (*Pclo*$^{wt/wt}$ = 179.7 μs ± 11.84, n = 18 cells;
1056 *Pclo*$^{gt/gt}$ = 172.2 μs ± 7.366, n = 23 cells; n = 3 rats per genotype; Mann-Whitney U test, *p* =
1057 0.866), the amplitude of the action potential (*Pclo*$^{wt/wt}$ = 67.85 mV ± 3.016, n = 18 cells; *Pclo*$^{gt/gt}$ =
1058 63.92 mV ± 2.761, n = 23 cells; n = 3 rats per genotype; Mann-Whitney U test, *p* = 0.291) and the
1059 voltage threshold to elicit an action potential (*Pclo*$^{wt/wt}$ = -51.27 mV ± 1.748, n = 18 cells; *Pclo*$^{gt/gt}$
1060 = -48.6 mV ± 1.659, n = 23 cells; n = 3 rats per genotype; Mann-Whitney U test, *p* = 0.162).

1061 C) Miniature excitatory postsynaptic currents from *Pclo*$^{gt/gt}$ GCs were not different in their
1062 amplitude (*Pclo*$^{wt/wt}$ = -19.62 pA ± 1.682, n = 15 cells; *Pclo*$^{gt/gt}$ = -22.44 pA ± 1.765, n = 23 cells;
1063 n = 3 rats per genotype; Mann-Whitney U test, p = 0.286) but in their frequency (*Pclo*$^{wt/wt}$ = 0.102
1064 Hz ± 0.0167, n = 15 cells; *Pclo*$^{gt/gt}$ = 0.257 Hz ± 0.0481, n = 22 cells; n = 3 rats per genotype;
1065 Mann-Whitney U test, p^* = 0.0392).
1066 D) Excitatory postsynaptic currents from GCs measured after stimulation of single mossy fibers
1067 were increased in *Pclo*$^{gt/gt}$ compared to *Pclo*$^{wt/wt}$ (*Pclo*$^{wt/wt}$ = 47.58 pA ± 12.12, n = 13 cells;
1068 *Pclo*$^{gt/gt}$ = 67.62 pA ± 9.64, n = 15 cells; n = 3 rats per genotype; Mann-Whitney U test, p^* =
1069 0.0356), whereas the decay of the EPSC was not alerted (*Pclo*$^{wt/wt}$ = 1.79 ms ± 0.258, n = 12 cells;
1070 *Pclo*$^{gt/gt}$ = 1.404 ms ± 0.141, n = 14 cells; n = 3 rats per genotype; Mann-Whitney test U, p^* =
1071 0.231). Right hand panel: example traces of evoked EPSCs, as quantified in D), in response 1 Hz
1072 stimulation in the presence of 20 µM SR95531 and 40 µM D-(2R)-amino-5-phosphonovaleric
1073 acid (D-APV).
1074 Scale bar = 20 µm (A). Error bars represent SEM. Data points represent individual cells from 3
1075 rats per genotype.
1076
1077 **Figure 10.** Behavioral outcome of Piccolo loss of function resembles PCH3 symptoms.
1078 A) Rotarod performance for *Pclo*$^{wt/wt}$, *Pclo*$^{wt/gt}$ and *Pclo*$^{gt/gt}$ rats for 16 trials over 4 days. *Pclo*$^{gt/gt}$
1079 rats fell significantly faster than *Pclo*$^{wt/wt}$ on trials 6 and 8 and faster than both *Pclo*$^{wt/wt}$ and
1080 *Pclo*$^{wt/gt}$ on trials 9-16 (trial 6: *Pclo*$^{wt/wt}$ = 56.25 s ± 5.023, *Pclo*$^{gt/gt}$ = 3.5 ± 0.5, p^* = 0.0293; trial 8:
1081 *Pclo*$^{wt/wt}$ = 65.25 s ± 18.688, *Pclo*$^{gt/gt}$ = 4.5 ± 0.957, p^{**} = 0.0042; trial 9: *Pclo*$^{wt/wt}$ = 63.25 s ±
1082 16.163, *Pclo*$^{wt/gt}$ = 61.5 s ± 18.319, *Pclo*$^{gt/gt}$ = 3.25 ± 0.75, p^{**} = 0.0051, $p^{\#\#}$ = 0.0079 (where * =
1083 p value between *Pclo*$^{wt/w}$ and *Pclo*$^{gt/gt}$ and $^{\#}$ = p value between *Pclo*$^{wt/wt}$ and *Pclo*$^{wt/gt}$); trial 10:
1084 *Pclo*$^{wt/wt}$ = 84.5 s ± 6.225, *Pclo*$^{wt/gt}$ = 60.25 s ± 18.396, *Pclo*$^{gt/gt}$ = 2.5 ± 0.5, p^{****} = <0.0001, $p^{\#\#}$ =
1085 0.0089; trial 11: *Pclo*$^{wt/wt}$ = 72 s ± 5.339, *Pclo*$^{wt/gt}$ = 76.75 s ± 12.419, *Pclo*$^{gt/gt}$ = 3 ± 0.408, p^{***} =
1086 0.0005, $p^{\#\#\#}$ =0.001; trial 12: *Pclo*$^{wt/wt}$ = 71 s ± 6.178, *Pclo*$^{wt/gt}$ = 68.75 s ± 9.681, *Pclo*$^{gt/gt}$ = 4 ±

0.707, $p^{***} = 0.0008$, $p^{\#\#} = 0.0015$; trial 13: $Pclo^{wt/wt}$ = 59 s ± 8.297, $Pclo^{wt/gt}$ = 57.75 s ± 12.99, $Pclo^{gt/gt}$ = 2.5 ± 0.5, $p^{*} = 0.0121$, $p^{\#} = 0.0164$; trial 14: $Pclo^{wt/wt}$ = 69.25 s ± 12.479, $Pclo^{wt/gt}$ = 61 s ± 13.638, $Pclo^{gt/gt}$ = 2.5 ± 0.645, $p^{***} = 0.0009$, $p^{\#\#} = 0.0074$; trial 15: $Pclo^{wt/wt}$ = 60.5 s ± 16.297, $Pclo^{wt/gt}$ = 65 s ± 18.757, $Pclo^{gt/gt}$ = 1.75 ± 0.479, $p^{**} = 0.0070$, $p^{\#\#} = 0.0022$; trial 16: $Pclo^{wt/wt}$ = 56.5 s ± 16.775, $Pclo^{wt/gt}$ = 68.75 s ± 17.109, $Pclo^{gt/gt}$ = 2.25 ± 0.25, $p^{*} = 0.0207$, $p^{\#\#\#} = 0.009$; n = 4 animals per genotype; two-way ANOVA with Bonferroni correction).

B) Grip strength task for $Pclo^{wt/wt}$, $Pclo^{wt/gt}$ and $Pclo^{gt/gt}$ rats for 9 trials over 2 days. No differences were found for forelimb grip strength between the groups. ($Pclo^{wt/wt}$ = 737.2 ± 109.9; $Pclo^{wt/gt}$ = 621.2 ± 93.46, $Pclo^{gt/gt}$ = 757.5 ± 66.74; n = 4 rats per genotype, one-way ANOVA, $p = 0.549$).

C) Ladder walk task for $Pclo^{wt/wt}$, 859 $Pclo^{wt/gt}$ and $Pclo^{gt/gt}$ rats for 3 trials over 1 day. $Pclo^{gt/gt}$ rats had a higher rate of stepping errors (ladder rung foot slips/misses) than $Pclo^{wt/wt}$ and $Pclo^{wt/gt}$ rats (forelimb error/step: $Pclo^{wt/wt}$ = 0.09 ± 0.00925, $Pclo^{wt/gt}$ = 0.148 ± 0.0263, $Pclo^{gt/gt}$ = 0.297 ± 0.0145, n = 4, one-way ANOVA, $p^{**} = 0.002$, $p^{\#} = 0.0157$ (where * = p value between $Pclo^{wt/w}$ and $Pclo^{gt/gt}$ and $^{\#}$ = p value between $Pclo^{wt/wt}$ and $Pclo^{wt/gt}$); hindlimb error/step: $Pclo^{wt/wt}$ = 0.0563 ± 0.0221, $Pclo^{wt/gt}$ = 0.0663 ± 0.00877, $Pclo^{gt/gt}$ = 0.238 ± 0.0543, n = 4; one-way ANOVA with Bonferroni correction, $p^{*} = 0.0135$, $p^{\#} = 0.0186$).

D) Open field task for $Pclo^{wt/wt}$, $Pclo^{wt/gt}$ and $Pclo^{gt/gt}$ rats for 1 trial each over 1 day. $Pclo^{gt/gt}$ rats performed fewer rearing behaviors than $Pclo^{wt/wt}$ and significantly less than $Pclo^{wt/gt}$ rats in the perimeter sectors of the arena ($Pclo^{wt/wt}$ = 64.25 ± 18.31 events; $Pclo^{wt/gt}$ = 76.25 ± 11.3 events; $Pclo^{gt/gt}$ = 22 ± 4.203 events; n = 4 rats per genotype, one-way ANOVA with Bonferroni correction, $p^{\#} = 0.0427$ (where $^{\#}$ = p value between $Pclo^{wt/wt}$ and $Pclo^{wt/gt}$). Other behaviors such as crossing the open field and grooming were not different between the three groups (crossing: $Pclo^{wt/wt}$ = 178.3 ± 29.68 events; $Pclo^{wt/gt}$ = 164.5 ± 45.51 events; $Pclo^{gt/gt}$ = 235.5 ± 27.11 events, n = 4 rats per genotype, one-way ANOVA with Bonferroni correction, $p = 0.828$; grooming: $Pclo^{wt/wt}$ = 2.75 ± 0.75 events; $Pclo^{wt/gt}$ = 2 ± 1.08 events; $Pclo^{gt/gt}$ = 5 ± 1.155 events, n = 4 rats per genotype, one-way ANOVA with Bonferroni correction, $p = 0.488$)

1113 E). Locomotor activity of *Pclo*$^{wt/wt}$, *Pclo*$^{wt/gt}$ and *Pclo*$^{gt/gt}$ rats during the 12h dark phase. *Pclo*$^{gt/gt}$

1114 rats covered a more than 50% longer distance than *Pclo*$^{wt/wt}$ and *Pclo*$^{wt/gt}$ rats (*Pclo*$^{wt/wt}$ = 135.7 ±

1115 11.25, n = 10; *Pclo*$^{wt/gt}$ = 129.3 ± 10.44, n = 4; *Pclo*$^{gt/gt}$ = 217.8 ± 14.33, n = 12; one-way

1116 ANOVA, p^{***} = 0.0002). Data points are individual means over 15 nights.

1117 F) Performance of *Pclo*$^{wt/wt}$, *Pclo*$^{wt/gt}$ and *Pclo*$^{gt/gt}$ rats during the isometric pull-task (handle

1118 position 11 mm inside the cage). Only 4 out of 11 *Pclo*$^{gt/gt}$ rats succeeded at the 60 g force

1119 threshold and *Pclo*$^{gt/gt}$ rats pulled with a significantly lower success rate at all force thresholds as

1120 compared to *Pclo*$^{wt/wt}$ and *Pclo*$^{wt/gt}$. (30g: *Pclo*$^{wt/wt}$ = 86.722 ± 2.3, n = 10; *Pclo*$^{wt/gt}$ = 84.374 ±

1121 6.324, n=4; *Pclo*$^{gt/gt}$ = 61.044 ± 5.928, n = 11; 2 way ANOVA with Bonferroni correction, p^{**} =

1122 0.0018; 40g: *Pclo*$^{wt/wt}$ = 83.603 ± 2.86, n = 10; *Pclo*$^{wt/gt}$ = 85.136 ± 7.373, n=4; *Pclo*$^{gt/gt}$ = 47.804 ±

1123 6.897, n = 10; two-way ANOVA with Bonferroni correction, p^{****} < 0.0001, $p^{\#\#\#}$ = 0.0007; 50g:

1124 *Pclo*$^{wt/wt}$ = 80.49 ± 3.442, n = 10; *Pclo*$^{wt/gt}$ = 71.930 ± 8.695, n=4; *Pclo*$^{gt/gt}$ = 33.647 ± 6.802, n =

1125 10; two-way ANOVA with Bonferroni correction, p^{****} < 0.0001, $p^{\#\#\#}$ = 0.0005 60g: *Pclo*$^{wt/wt}$ =

1126 69.186 ± 4.99, n = 10; *Pclo*$^{wt/gt}$ = 70.409 ± 10.181, n=3; *Pclo*$^{gt/gt}$ = 30.003 ± 11.359, n = 4; 2 way

1127 ANOVA with Bonferroni correction, p^{***} = 0.0004, $p^{\#\#}$ = 0.0056).

1128 Error bars represent SEM. Data points represent individual rats.

Figure 1

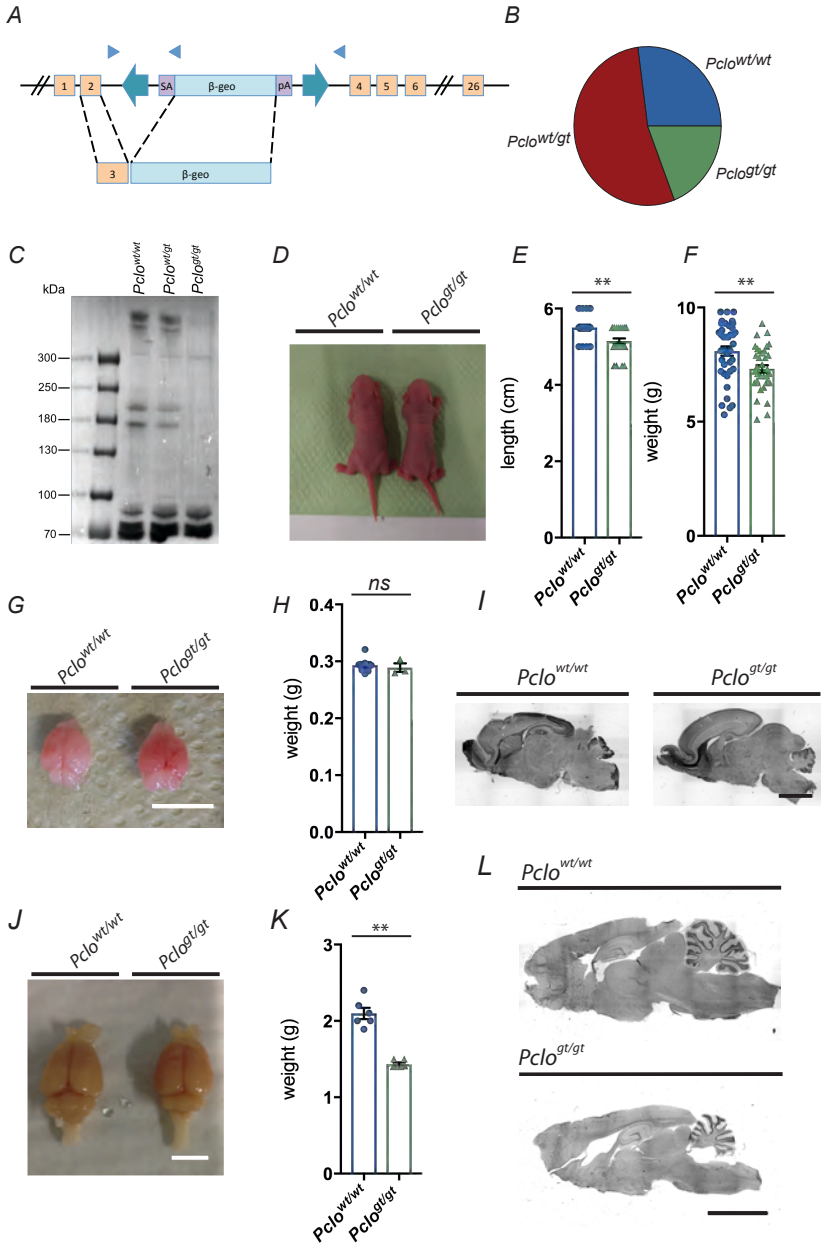
A
1
2
SA
β-geo
pA
4
5
6
26
3
β-geo
B
Pclo wt/wt
Pclo wt/gt
Pclo gt/gt
C
kDa
Pclo wt/wt
Pclo wt/gt
Pclo gt/gt
300
250
180
130
100
70
D
Pclo wt/wt
Pclo gt/gt
E
**
length (cm)
Pclo wt/wt
Pclo gt/gt
F
**
weight (g)
Pclo wt/wt
Pclo gt/gt
G
Pclo wt/wt
Pclo gt/gt
H
ns
weight (g)
Pclo wt/wt
Pclo gt/gt
I
Pclo wt/wt
Pclo gt/gt
J
Pclo wt/wt
Pclo gt/gt
K
**
weight (g)
Pclo wt/wt
Pclo gt/gt
L
Pclo wt/wt
Pclo gt/gt

Figure 2

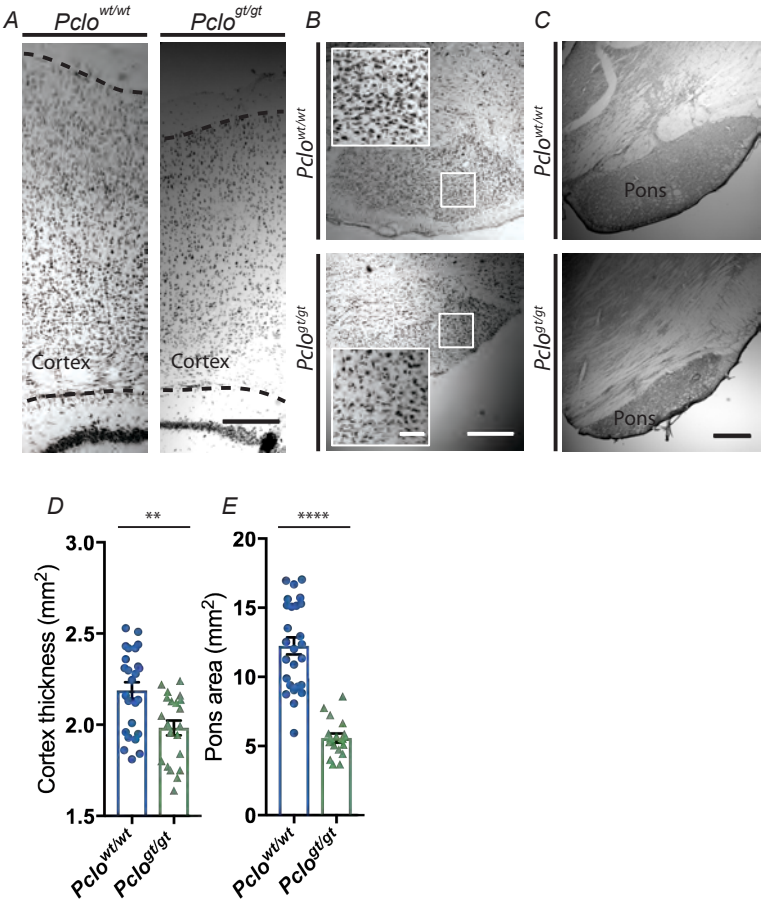
A
Pclo wt/wt
Pclo gt/gt
Cortex
Cortex
B
Pclo wt/wt
Pclo gt/gt
C
Pclo wt/wt
Pclo gt/gt
Pons
Pons
D
**
Cortex thickness (mm2)
3.0
2.5
2.0
1.5
Pclo wt/wt
Pclo gt/gt
E
****
Pons area (mm2)
20
15
10
5
0
Pclo wt/wt
Pclo gt/gt

Figure 3

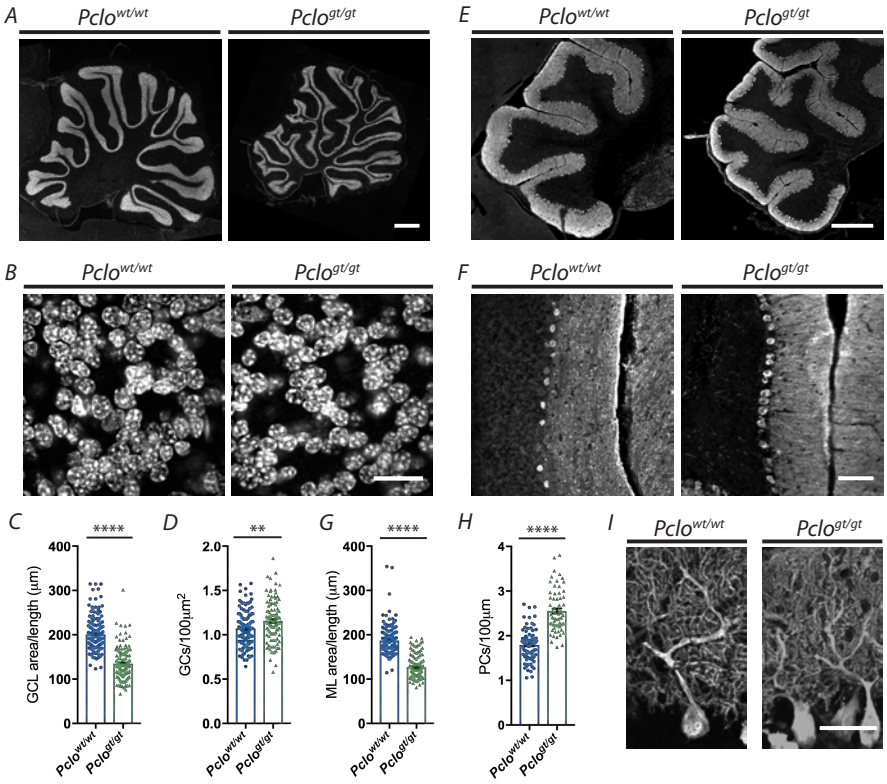
A
Pclo wt/wt
Pclo gt/gt
E
Pclo wt/wt
Pclo gt/gt
B
Pclo wt/wt
Pclo gt/gt
F
Pclo wt/wt
Pclo gt/gt
C
****
GCL area/length (µm)
400
300
200
100
0
Pclo wt/wt
Pclo gt/gt
D
**
GCs/100µm2
2.0
1.5
1.0
0.5
0.0
Pclo wt/wt
Pclo gt/gt
G
****
ML area/length (µm)
400
300
200
100
0
Pclo wt/wt
Pclo gt/gt
H
****
PCs/100µm
4
3
2
1
0
Pclo wt/wt
Pclo gt/gt
I
Pclo wt/wt
Pclo gt/gt

Figure 4

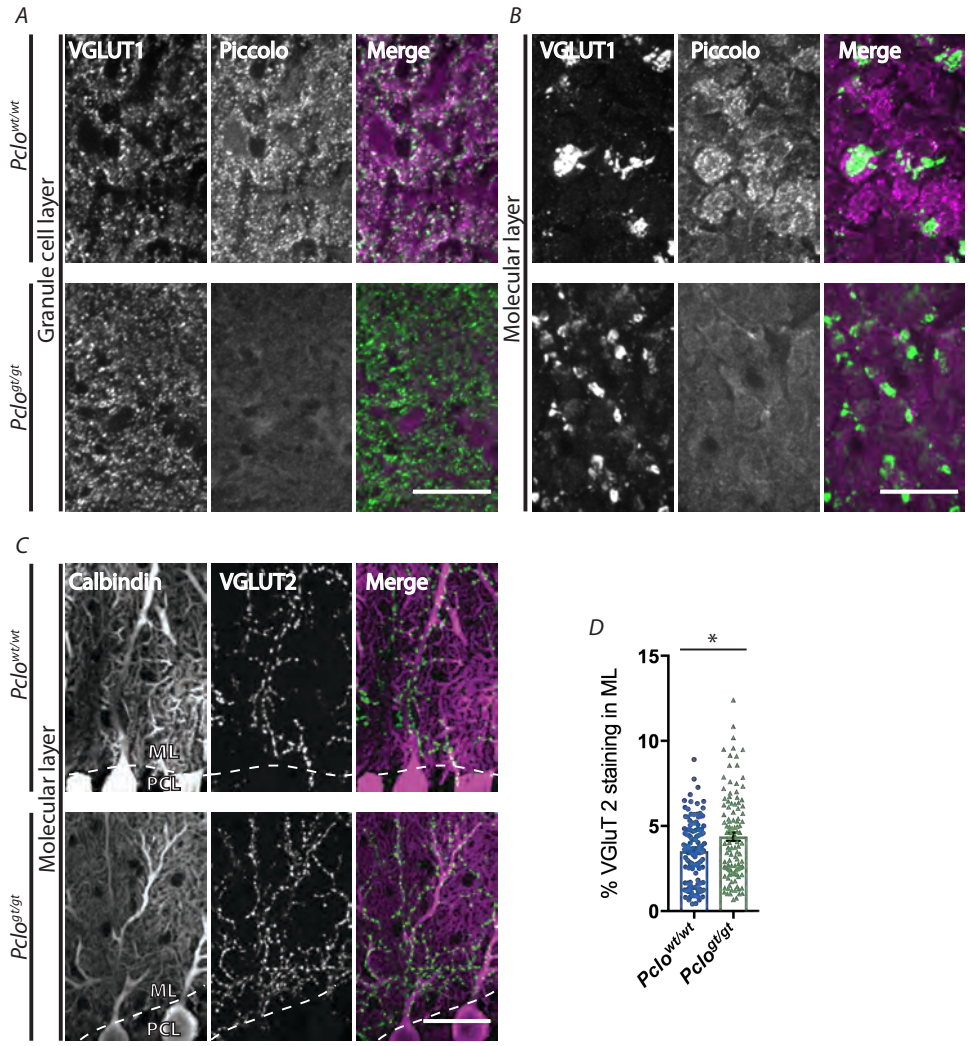
A
VGLUT1
Piccolo
Merge
Pclo wt/wt
Pclo gt/gt
Granule cell layer
B
VGLUT1
Piccolo
Merge
Molecular layer
C
Calbindin
VGLUT2
Merge
Pclo wt/wt
Pclo gt/gt
Molecular layer
ML
PCL
ML
PCL
D
*
% VGluT 2 staining in ML
15
10
5
0
Pclo wt/wt
Pclo gt/gt

Figure 5

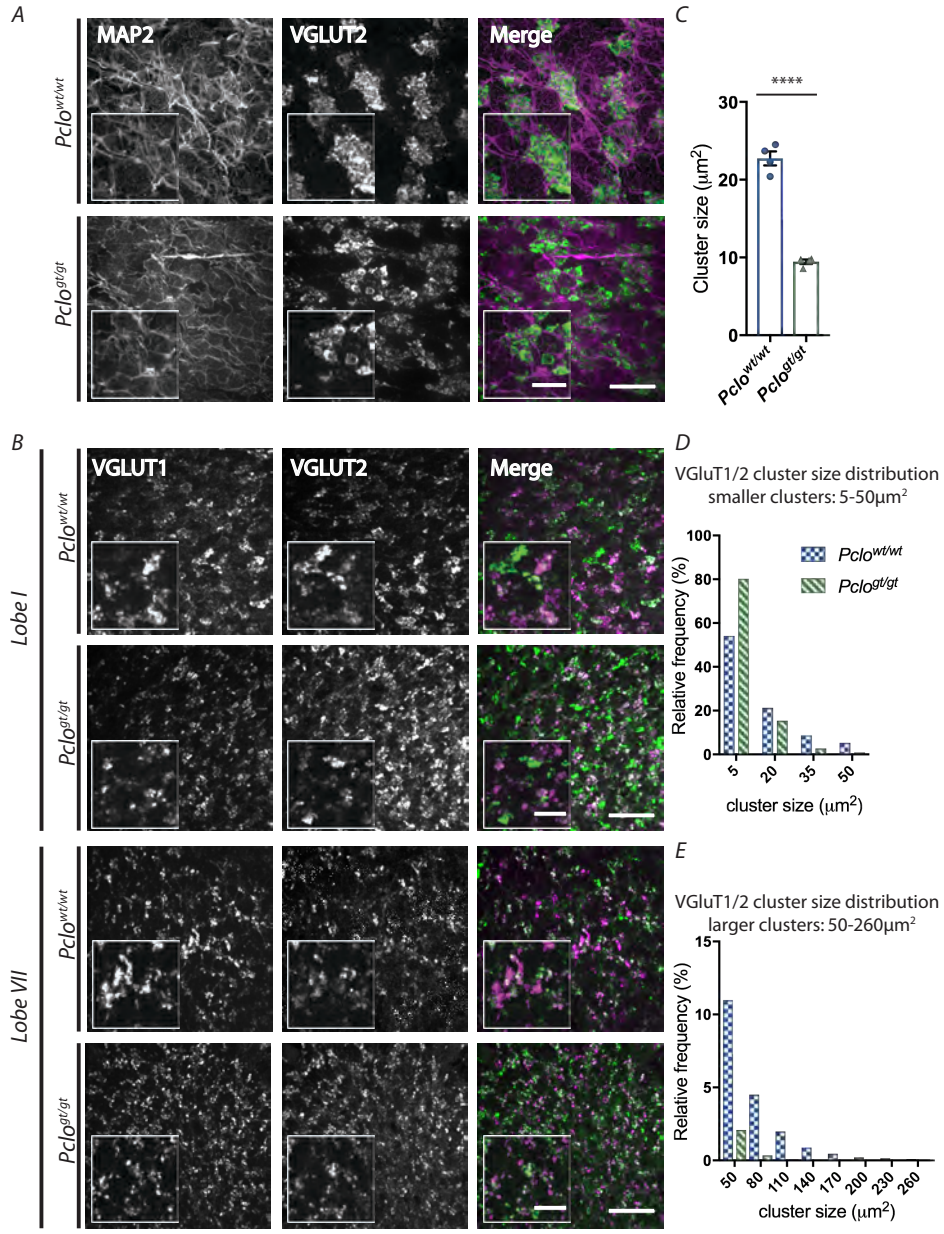
A
MAP2
VGLUT2
Merge
Pclo wt/wt
Pclo gt/gt
C
****
Cluster size (μm²)
30
20
10
0
Pclo wt/wt
Pclo gt/gt
B
VGLUT1
VGLUT2
Merge
Lobe I
Lobe VII
D
VGluT1/2 cluster size distribution
smaller clusters: 5-50μm²
Relative frequency (%)
100
80
60
40
20
0
5
20
35
50
cluster size (μm²)
E
VGluT1/2 cluster size distribution
larger clusters: 50-260μm²
15
10
5
0
50
80
110
140
170
200
230
260

Figure 6

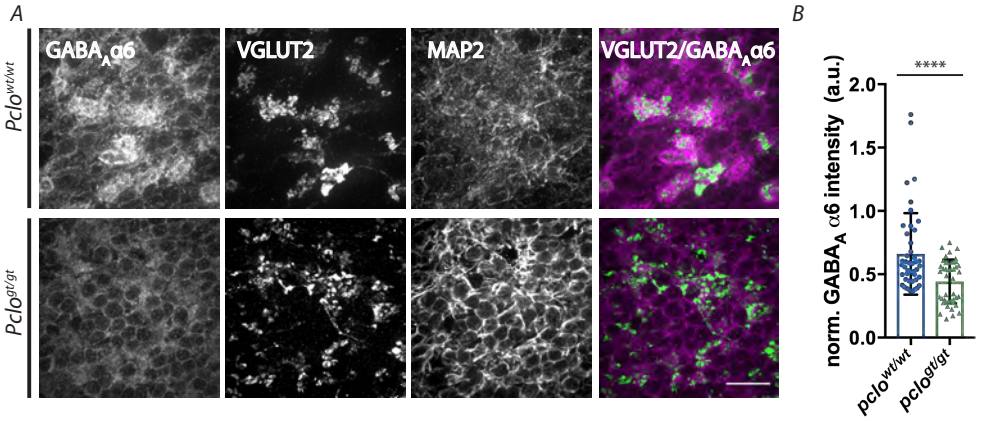
A
B
GABA$_A$α6
VGLUT2
MAP2
VGLUT2/GABA$_A$α6
Pclo$^{wt/wt}$
Pclo$^{gt/gt}$
****
norm. GABA$_A$ α6 intensity (a.u.)
2.0
1.5
1.0
0.5
0.0
pclo$^{wt/wt}$
pclo$^{gt/gt}$

Figure 7

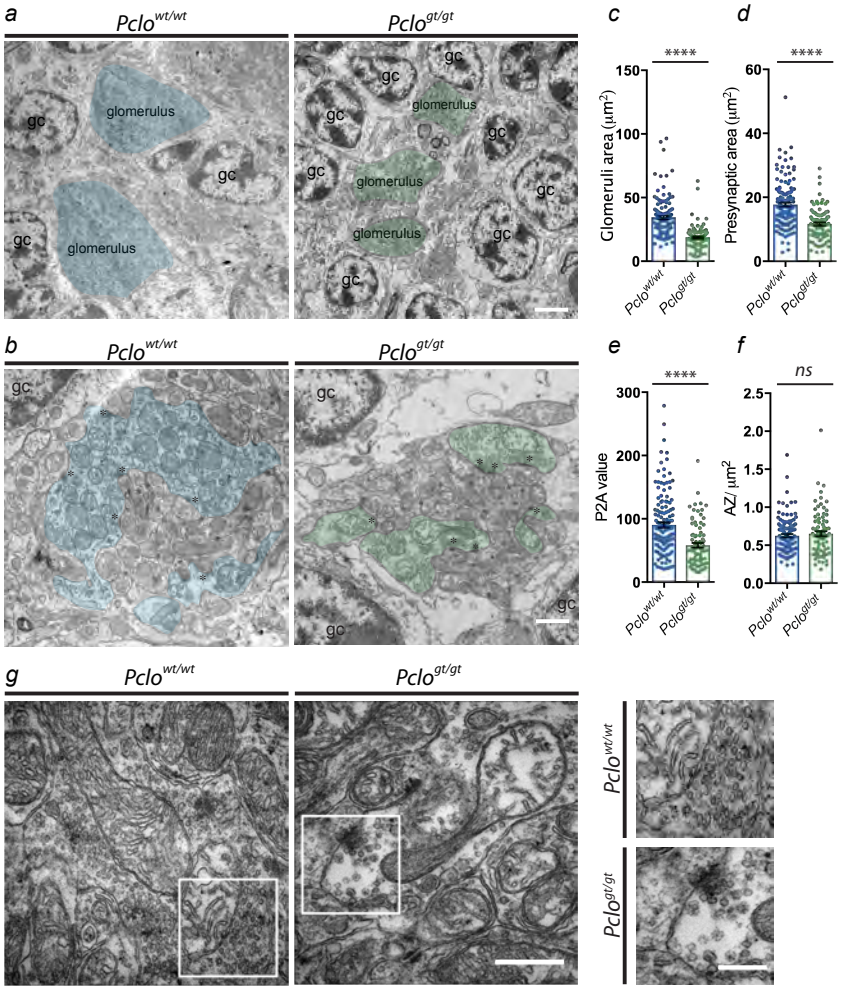
a
Pclo wt/wt
Pclo gt/gt
glomerulus
gc
b
g
c
d
e
f
****
ns
Glomeruli area (µm²)
Presynaptic area (µm²)
P2A value
AZ/ µm²
Pclo wt/wt
Pclo gt/gt

Figure 8

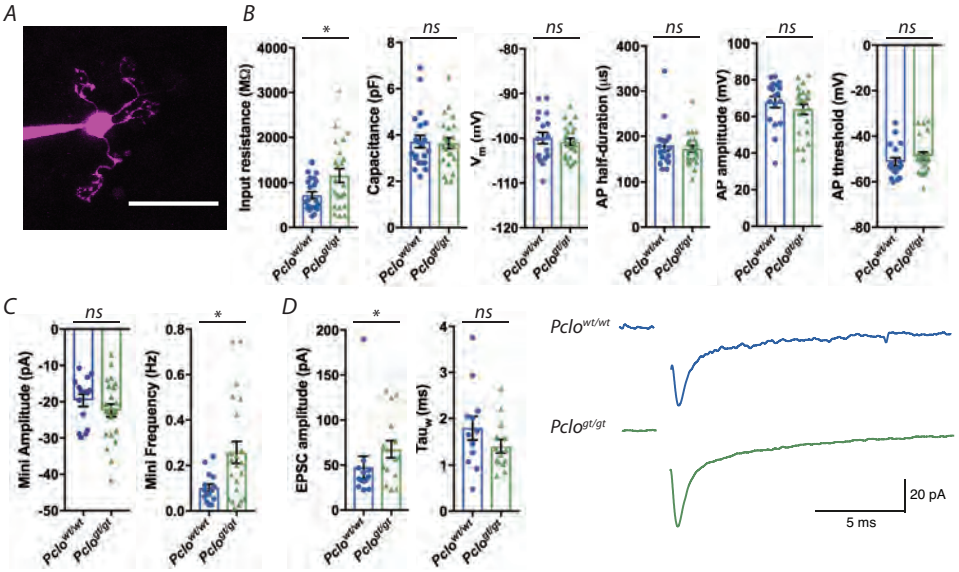

A
B
C
D
Input resistance (MΩ)
Capacitance (pF)
V_m (mV)
AP half-duration (µs)
AP amplitude (mV)
AP threshold (mV)
Mini Amplitude (pA)
Mini Frequency (Hz)
EPSC amplitude (pA)
Tau_w (ms)
*
ns
$Pclo^{wt/wt}$
$Pclo^{gt/gt}$
20 pA
5 ms

Figure 9

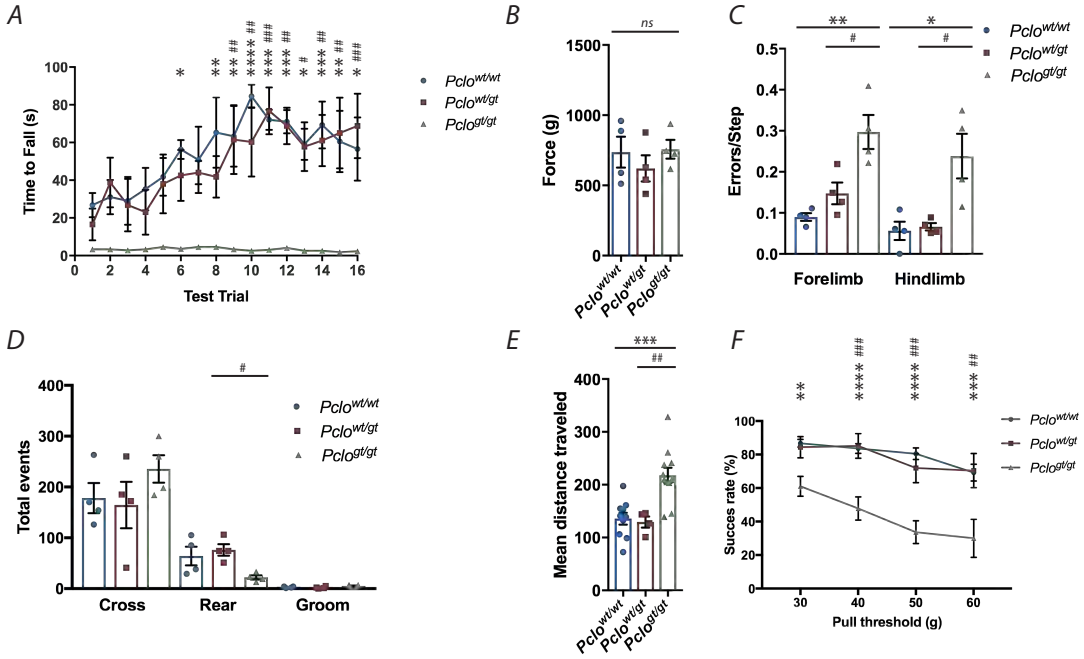
A
Time to Fall (s)
Test Trial
Pclo wt/wt
Pclo wt/gt
Pclo gt/gt
B
Force (g)
ns
C
Errors/Step
Forelimb
Hindlimb
D
Total events
Cross
Rear
Groom
E
Mean distance traveled
F
Succes rate (%)
Pull threshold (g)